Composites: Part A 180 (2024) 108042

Contents lists available at ScienceDirect

Composites Part A

journal homepage: www.elsevier.com/locate/compositesa

# A progressive micromechanical model for single-polymer composites and experimental validation on self-reinforced PA6-based composites

S.K. Jalali [a], G. Greco [a], D. Rigotti [b], A. Dorigato [b], H. Mirbaha [a], G. Fredi [b], M. Bertolla [c], S. Guerra [c], T. Battistini [c], A. Dal Moro [c], A. Pegoretti [b], N.M. Pugno [a,d,*]

[a] Laboratory for Bioinspired, Bionic, Nano, Meta Materials and Mechanics, Department of Civil, Environmental and Mechanical Engineering, University of Trento, Italy

[b] Department of Industrial Engineering and INSTM Research Unit, University of Trento, Via Sommarive 9, 38123 Trento, Italy

[c] Aquafil S.p.A., via Linfano 9, 38062 Arco, Trento, Italy

[d] School of Engineering and Materials Science, Queen Mary University of London, Mile End Road, London E1 4NS, UK

ARTICLE INFO

*Keywords:*
A. Polymer (textile) fibres
B. Analytical modeling
C. Damage mechanics C. Statistical properties/methods
Single Polymer Composites (SPCs)

ABSTRACT

The current paper proposes a novel analytical micromechanics model to progressively predict the mechanical behavior of composites reinforced by continuous or discontinuous aligned fibers considering the nonlinear mechanical behavior of components and statistical breakage of fiber bundles based on the Curtin model. The PA6-based Single polymer composites (SPCs) are selected and extensive sets of experimental measurements on 12 available PA6 fibers with adequate repetitions to find reliable statistical Weibull parameters are performed. In addition, 10 different PA6 matrix samples, polymerized with various dosages of additives and raw materials, are tested. A remarkable potential for enhancing both strength and toughness of neat PA6 matrix is demonstrated. Results reveal that using tough matrices with elongation in the order of PA6 fibers significantly enhances both strength and toughness of the SPC. The developed progressive micromechanics model provides an analytical parametric framework and a design guideline for developing new recyclable SPCs.

## 1. Introduction

The demand for polymers as replacements for wood, metals, and ceramics is steadily increasing due to their unique low weight on the side of relatively low-cost manufacturing processes. Characterized by inferior mechanical properties, polymers normally need to be reinforced when used in loading bearing components in automotive, marine, medical, sport, construction, and aerospace industries [1,2]. The valuable extensive history of polymeric composite materials proves the successful use of traditional reinforcements, mostly glass, carbon, and Kevlar® fibers, on the scale of industrial mass production [3]. Although excellent mechanical properties can be achieved, however, the unsolved challenge of recycling at the end of the life-cycle limits their immense continued production considering environmental impacts since these fibers are almost impossible to be recycled. To overcome this, the composite community performed vast research and developments on alternatives to replace traditional reinforcement. Subsequently, biodegradable composites implementing natural fibers and even bio-based polymers [4], and nano-composites [5,6] relying on the idea of reinforcing polymers with a low percentage of nanoparticles with high surface-to-volume ratios emerged. Despite successful developments of these modern composites especially in the automotive and aerospace sectors, they could not take the place of a large amount of mass production of traditional composites, especially those made of carbon and glass fibers, due to economic and technical issues. In addition, the biodegradable composites made from natural fibers are not mechanically recyclable as the fiber and the matrix are not the same/similar material. The increasing importance of environmental legislation and waste management regulations, considering the limited landfill space, and thinking of global warming which is affected by incinerator emissions, encourage both researchers and industries in the field of composite to look for effective recyclable composites, without sacrificing the primary goal of developing composites, i.e., enhancement in mechanical properties [7,8]. Furthermore, introducing new easy-recyclable composites can improve the efficiency of the recycling process in terms of energy consumption, which is conceivable from an economic point of view [9,10].

Keeping in mind the fact that the main challenge in the recycling of traditional composite is the fiber since the polymeric thermoplastic matrix can be melted and extracted, one may think of implementing

* Corresponding author.
*E-mail address:* nicola.pugno@unitn.it (N.M. Pugno).

https://doi.org/10.1016/j.compositesa.2024.108042
Received 25 July 2023; Received in revised form 18 January 2024; Accepted 20 January 2024
Available online 24 January 2024
1359-835X/© 2024 The Author(s). Published by Elsevier Ltd. This is an open access article under the CC BY-NC-ND license (http://creativecommons.org/licenses/by-nc-nd/4.0/).

polymeric fibers resulting in the concept of environmentally friendly all-polymeric or polymer–polymer composites (PPCs) [11]. The PPC concept becomes more logical when considering that the mechanical properties of components are reduced after each re-extrusion. Having a base material similar to the matrix, polymeric fibers provide superior mechanical properties thanks to their highly oriented molecular structure with a high degree of crystallinity which is achieved by spinning or solid-state drawing manufacturing techniques [12]. On the other hand, similarity in the chemical composition of the fiber and the matrix allows for the formation of strong chemical bonding and enhanced interfacial adhesion without any surface treatment as a result of molecular entanglements and possible H-bonding which increases the stress transfer capacity of the interface [13]. It surmounts the classical problem of weak interface and debonding failure in the conventional composite where the fiber and the matrix possess quite different chemical composition and surface energies and weak van der Waals forces act across the interfacial region. In conclusion, proposing satisfactory mechanical properties, high recyclability, strong interfacial bonding along with low density (even less than carbon fibers) and remarkable performance/cost balance make polymeric fibers ideal for replacing traditional fibers. A wide selection of high-performance polymeric fibers such as PE, PT, PET, PP, iPP, PLA, PA6, PA6.6, PMMA, etc., with a performance comparable to traditional fibers, are available to be combined with thermoplastic polymeric matrices leading to fully recyclable PPCs [14].

In general, PPCs consist of two different polymers which are from the same family. As a subset of PPCs, single polymer composites (SPCs) are composed of the exactly same polymer or of polymers belonging to the same type. SPCs are also known as one-polymer, self-reinforced, or homo-composites. Referring to the composite material definition, despite the same base material of the components, the highly anisotropic arrangement of molecular structure in the fiber serves for reinforcement while the matrix with mostly isotropic, due to randomly oriented molecular structures, transfers the load. This combination enhances the mechanical properties of the SPC compared to the neat polymeric matrix [13]. From a recycling point of view, where with every re-extrusion the material quality undergoes a reduction, PPCs are melted down to a polymeric blend of the components, however, recycling of SPCs is essentially melting a single polymer [15]. It means SPCs are recycled to an almost single-phase homogeneous raw material which can be utilized for manufacturing a new SPC or be used as a matrix of a conventional composite or any other application [16]. Even though there is a potential for down-cycling of thermoplastic-based composites reinforced by traditional fibers, along with ongoing research focused on their up-cycling, SPCs can still be considered major alternatives due to their remarkable recycling characteristics and strong interfacial bonding advantages in various applications [17]. However, they suffer from the small temperature window during the manufacturing process because the fiber and the matrix have close melting temperatures [18]. In this situation, the main challenge is to retain the properties of the highly oriented polymer molecules of the fiber, since it tends to be relaxed approaching the melting temperature. It opens a window for the optimized design of SPCs since on the other hand it is reported that partial melting of the polymeric fibers before mixing can enhance the interfacial bonding [19]. It is essential to acknowledge that introducing polymeric fibers in SPCs typically has the potential to enhance the mechanical properties by a few times, whereas conventional composites utilizing Glass, Carbon, and Kevlar® fibers offer orders of magnitude increase in properties. Consequently, when the utmost performance is the primary consideration in composite design, replacing SPCs might not be always feasible. Another remarkable potential application for SPCs, especially those based on more economical polymers like PA6, could involve substituting other high-performance, expensive neat polymers such as PEEK.

The successful developments of SPCs with desirable mechanical properties are extensively reported confirming the potential of SPCs with superior recycling capacity as an alternative to conventional composites. A PA6-based SPC was made by combining hot compaction and film stacking techniques in [20]. The high-tenacity PA6 yarn as the reinforcement and PA6 film as the matrix are combined to make the SPC with a proper difference in the melting temperature of the components. The prepared layered self-reinforced composite shows superior mechanical properties where the tensile modulus and ultimate strength are improved by 200% and 300%–400%, respectively, compared to the isotropic matrix film. A PE-based SPC composed of UHMWPE fiber and UHMWPE matrix without using any chemical treatment was introduced in [21] and a remarkable interfacial bonding and a strength comparable to Kevlar®-resin composites were reported. It was also proved that the developed SPC provided better mechanical performance compared to the PPCs consisting of UHMWPE fibers and other polymeric matrices. Preparation and characterization of PP-based SPCs fabricated by the film-stack method were reported in [22] and the results revealed that controlling consolidation temperature and holding time can enhance the mechanical and morphological properties. A self-reinforced composite composed of a PMMA matrix reinforced by a high-strength PMMA fiber with desirable mechanical properties was introduced in [23] and the effect of processing temperature and time on the fracture toughness, morphology, and the thermal properties of this PMMA-based SPC were probed. They stated that the SPCs were fabricated using an anionic polymerization process, making re-extrusion impractical as a recycling solution, since depolymerization is the only viable recycling method. The advantage of depolymerization over re-extrusion is the ability to revert back to raw material without partial polymer degradation. The effect of hot compaction temperature on the crystallinity and molecular orientation of PET SPCs was investigated in [24] and it was observed that the impact strength of the SPC can be improved by 500%–700% compared to the neat PET matrix. A novel method based on the in-situ anionic polymerization was developed in [7] to fabricate the polyamide SPCs mixing a PA6 fiber and a PA6 matrix. The effect of process parameters and molding temperature on the performance of SPCs was studied. Performing three-point bending and tensile tests, an optimum molding temperature of 160 °C where both tensile strength and flexural strength are maximal was reported. Besides, a low fraction of voids and a strong fiber/matrix interface were reached.

Predicting the mechanical properties of polymeric composites has always been of great importance in designing and manufacturing durable optimized structures. The aim of all micromechanics models is to perform this duty by having the arrangement and mechanical properties of the constitutive materials as the input. Of course, knowing the effective elastic properties of composites is essential as the first step of the design and accordingly, a number of well-known micromechanics approaches such as the rule of mixture, the Halphin–Tsai equation, and the Mori–Tanaka model are developed for this purpose which is reviewed in detail in [25]. However, the evaluation of the failure of composites demands a more advanced complicated micromechanics model due to the complex nature of composites, progressive failure characteristics, and the existence of local nonlinear effects, such as damage, debonding, and inelasticity [26,27]. In consequence, a comprehensive fully validated model for the failure prediction of composite materials is difficult to achieve. From a microscopic point of view, the failure of composites may be led by fiber progressive breakage and then fiber pull-out, fiber/matrix debonding, matrix cracking, and delamination [28–30]. A comprehensive review of micromechanical progressive failure models in unidirectional fiber-reinforced composites is presented in [31].

The prediction of the effective elastic properties of SPCs can be performed by employing the general micromechanics model reviewed in [25], without any need for specific modifications. The only point is that the difference between the elastic properties of the fiber and the matrix in SPCs may not be comparable to that of carbon or glass fiber-reinforced composites and consequently, the effective properties of the

SPCs may remain in the same order of its constitutive components. However, predicting the failure of SPCs demands a more advanced specific model. This paper aims to propose a progressive micromechanics model exclusively developed to be applicable for predicting the mechanical behavior of SPCs reinforced by aligned fibers parallel to the applied unidirectional loading. The model considers inelastic behavior for both the fiber and the matrix, which is common in SPCs, by converting their nonlinear stress–strain curve to an approximated segmented piece-wise linear curve. Moreover, the classical shear lag is modified. Although the model is capable to introduce weak interfacial bonding, however, it does not consider the fiber/matrix debonding failure model which is reasonable in SPCs with strong chemical interfacial bonding. No delamination failure is introduced into the model since the SPC is assumed to be non-layered. The failure mechanism is defined as the competition between the progressive breakage of polymeric fibers and the matrix failure at its failure strain. The model also takes into account the fiber pull-out and its extra effect on the SPC toughness. To demonstrate the ability of the model to predict the properties of SPCs, first, a comprehensive experimental investigation on the properties of PA6 fiber and PA6 matrices is performed and imported to the model to evaluate the mechanical performance of PA6-based SPC as a case study. It is followed by a parametric study on the effect of interfacial bonding and experimental validation.

## 2. Development of the model

In this section, a progressive micromechanics model is proposed that estimates the stress–strain curve and consequently the stiffness, strength, and toughness of composites using the stress–strain curves of the components. It is developed based on the Curtin-stochastic fiber breakage model that applies Weibull strength statistics for fibers [32–36] along with a modified Kelly–Tyson shear-lag analysis [37] for better capturing the effect of the shape of cross section and non-uniformity in the interfacial shearing stress. Both continuous and discontinuous aligned fibers are considered.

### 2.1. Inputs of the model

First, the required inputs of the progressive model are defined and formulated. In the whole text, superscripts $f$, and $m$ denote the fiber and the matrix, respectively. Consider a composite consisting of fibers of volume fraction $v^f$ aligned parallel to the direction of an applied strain, $\varepsilon$. For the case of unbroken continuous fibers, the strain in both the matrix and the fibers are the same and equal $\varepsilon$, while for discontinuous or broken continuous fibers the applied strain is transferred to the fiber through a distance from the ends via interfacial shearing stress between the fibers and the matrix. In general, the stress–strain curves of the components are not linear, particularly for SPCs where both the fiber and the matrix are polymeric. The stress–strain curve of either the fiber or the matrix can be approximated as a combination of $N$ linear segments where for the $k$th segment the starting strain is $\varepsilon_k$ and the slope is $E_k$. Then, the stresses corresponding to the applied strain, $\varepsilon$, across the 1st segment, $\varepsilon_0 < \varepsilon < \varepsilon_1$, the 2nd segment, $\varepsilon_1 < \varepsilon < \varepsilon_2$, and generally the $k$th segment, $\varepsilon_{k-1} < \varepsilon < \varepsilon_k$, where $k = 3, 4, \ldots, N$, are approximated as:

$$\sigma_1(\varepsilon) = E_1(\varepsilon - \varepsilon_0) \tag{1a}$$

$$\sigma_2(\varepsilon) = E_1(\varepsilon_1 - \varepsilon_0) + E_2(\varepsilon - \varepsilon_1) \tag{1b}$$

$$\sigma_k(\varepsilon) = \sum_{j=1}^{j=k-1} \left(E_j(\varepsilon_j - \varepsilon_{j-1})\right) + E_k(\varepsilon - \varepsilon_{k-1}) \tag{1c}$$

This approximation is schematically shown in Fig. 1(a). At the ending point of the curve, the strain reaches the maximum, named the elongation at break or failure strain, denoted by $\varepsilon_N = e$, and the corresponding stress is the strength, denoted by $\sigma(e) = S$. Setting $k = N$ and $\varepsilon = e$ in Eq. (1), the expression for the strength in a segmented sense is obtained:

$$S = \sum_{k=1}^{k=N} E_k(\varepsilon_k - \varepsilon_{k-1}) \tag{2}$$

The toughness, $T$, is approximated as the area under the curve:

$$T = \frac{1}{2}\sum_{k=1}^{k=N} (\varepsilon_k - \varepsilon_{k-1})(\sigma(\varepsilon_k) + \sigma(\varepsilon_{k-1})) \tag{3}$$

Since it is assumed that the strength of fibers obeys the Weibull strength statistics, a reference strength and a reference elongation at break, $S_0^f$ and $e_0^f$, are introduced. The reference fiber length corresponding to $S_0^f$ is indicated as $l_0$. For a fiber with an arbitrary length $l$, the total number of flaws that are broken when the arbitrary stress $S^f$ is applied to the fiber is:

$$\phi(S^f, l) = \frac{l}{l_0}\left(\frac{S^f}{S_0^f}\right)^{\alpha} \tag{4}$$

and the cumulative probability of fiber failure of length $l$ at a given stress $S^f$ is determined by [35]:

$$P(S^f, l) = 1 - exp\left[-\frac{l}{l_0}\left(\frac{S^f}{S_0^f}\right)^{\alpha}\right] \tag{5}$$

where $\alpha$ is the "Weibull modulus", normally ranging from 2 to 20 corresponding to very brittle fibers with dispersed values of strength to ductile ones with a low dispersion. From Eq. (5) it can be obtained that for the reference conditions of $l = l_0$, and $S^f = S_0^f$, the cumulative probability of fiber failure is $P = 1 - 1/e = 0.63$. This implies that some fibers can break for higher stress values than $S_0^f$. This is considered in the stress–strain curve of the fibers by extending the $N$th segment with slope $E_N$, as shown in Fig. 1(b). For large values of Weibull modulus, $\alpha$, the scattering in the strength of fibers around the reference strength decreases resulting in a shorter dashed line in Fig. 1(b). In addition, Eqs. (4) and (5) reveal that not only is the fiber strength at a fixed length a statistically distributed quantity but also that the fiber strength is length dependent, as given by:

$$S_l^f = S_0^f\left(\frac{l_0}{l}\right)^{1/\alpha} \tag{6}$$

It is assumed that the initial strength, $S_0^m$, and the elongation at break, $e_0^m$ of the matrix before composition with the fibers, are not statistical variables, however, the possibility of adding an extra elongation is considered as a result of composition with the fibers which is experimentally observed in some references [12]. This extra elongation is included in the model by appending to the end of the approximated stress–strain curve of the matrix an extension to the $N$th segment, as depicted in Fig. 1(b).

### 2.2. Modified shear-lag analysis

Before developing the progressive micromechanics model, a modification to the classical Kelly–Tyson shear-lag equation is presented to better account for the shape of cross-section and non-uniformity in the distribution of interfacial shear stress. This equation is required for the evaluation of stresses along either the discontinuous or broken continuous fibers. Fig. 2 shows a fiber with an arbitrary cross-section shape, laid within a matrix media where the interfacial shearing stress, $\tau_{rz}(z)$, transfers the axial load to the fiber in the $z$ axis direction. If the origin of the $z$ axis is on the fiber tip, the axial load is zero at $z = 0$ and it increases along a load transferring length to reach a maximum value of $\sigma_{max}^f$ at $z = l_t$. As shown in Fig. 2(c), the cross-section of a fiber with an area $A$ and a perimeter $S$ can be surrounded by a circle of diameter $D$. From the equilibrium along the fiber axis, the axial stress carried by

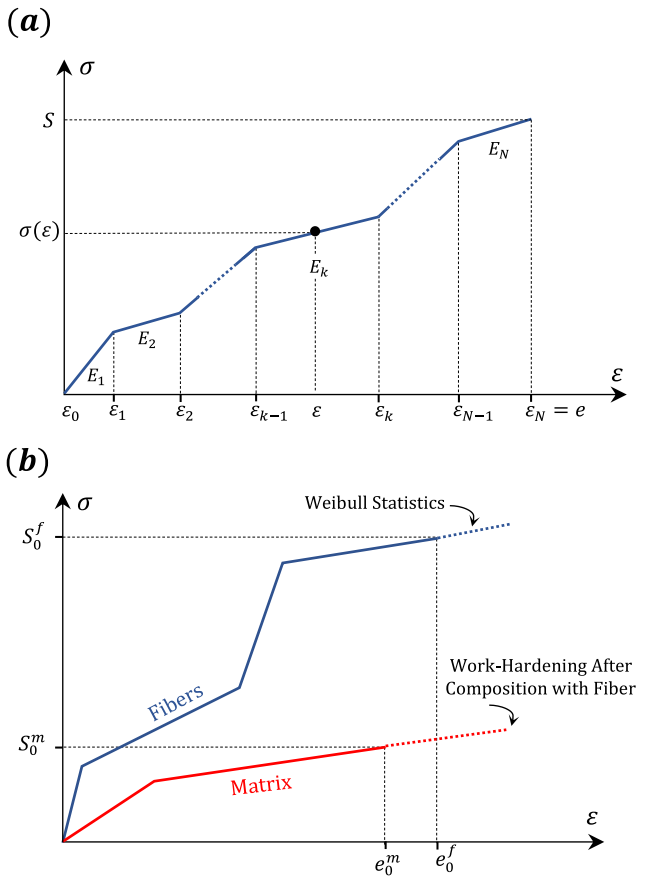


**Fig. 1.** The schematic of the approximated stress–strain curve with $N$ linear segments.

the fiber over the transferring length can be related to the interfacial shear using the equation:

$$\frac{d\sigma_z^f(z)}{dz}A = S\bar{\tau}_{rz} \rightarrow \sigma_z^f(z) = \left(\frac{S}{A}\right)\int_0^z \bar{\tau}_{rz}(z)\,dz \tag{7}$$

Lacking symmetry in a general non-circular cross-section, the interfacial shear $\tau_{rz}(z)$ is not uniform within the $rz$ planes and therefore it is replaced with its average, $\bar{\tau}_{rz}(z)$ in Eq. (7). The perimeter-to-area ratio of the fiber, $S/A$, depends on the geometry, and it has its minimum value $(S/A)_{min} = 4/D$ for a circular cross-section. For any arbitrary cross-section, this ratio is larger:

$$(S/A) = \gamma(S/A)_{min} = \gamma(4/D) \tag{8}$$

The values of the cross-section correction factor, $\gamma \geq 1$, are presented for some typical cross-sections in Fig. 3 and plotted in Fig. 4. For $n$-sided regular polygons it varies between $\gamma = 1$ for circular ($n \rightarrow \infty$) and $\gamma = 2$ for triangular ($n = 3$). For an elliptical cross-section $\gamma = 1$ where the aspect ratio $r = D/t = 1$ (circular) and it increases by increasing $r$, while for a rectangular cross-section, the correction factor is $\gamma = \sqrt{2}$ where the aspect ratio is $r = w/t = 1$ (square) and it increases by increasing $r$. The correction factor of the elliptical cross-section remains lower than the rectangular one until the aspect ratio $r_2 \approx 2.86$ and then for $r > r_2$, the elliptical overs. The 3-pointed star cross-section turns to a hexagonal when its aspect ratio is minimum, i.e., $r = D/t = 2/\sqrt{3}$ with $\gamma = 2/\sqrt{3}$. Its correction factor increases by increasing the aspect ratio, $r$. It is always higher than the elliptical cross-section for all aspect ratios, however, it is lower than rectangular for $r < r_1 \approx 1.86$. For $r > r_1$ the 3-pointed star cross-section has the highest $\gamma$ among all the other mentioned cross-sections for a given $r$. It is important to note that the efficient packing capabilities inherent in cross-sectional shapes, such as rectangular, square, or hexagonal fiber cross-sections, play a pivotal role in achieving high fiber volume fractions and, consequently,

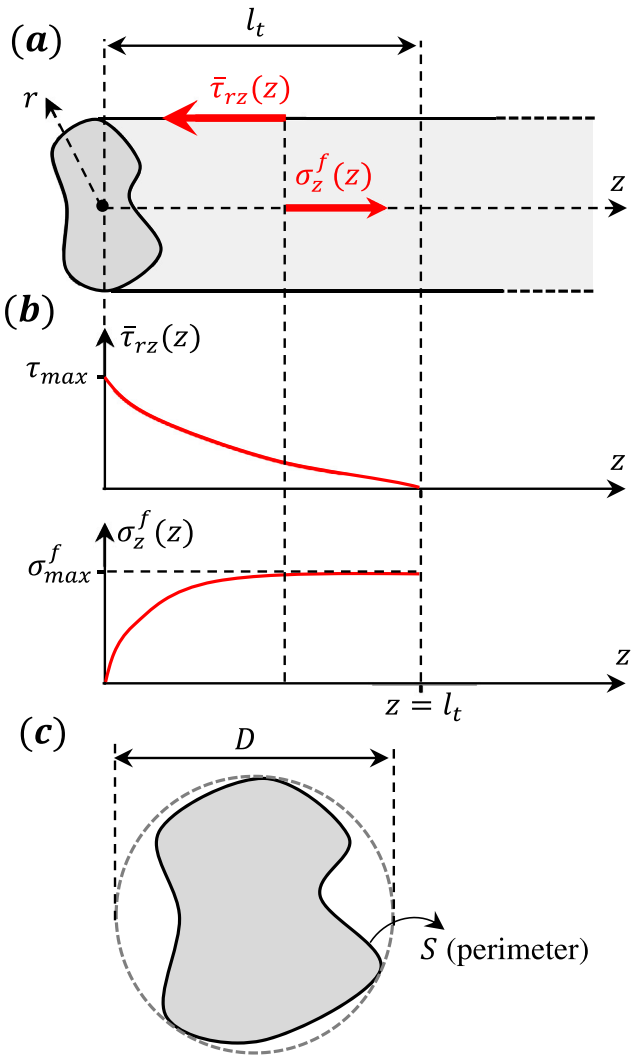


**Fig. 2.** Modified shear-lag equation. (a) The equilibrium of the interfacial shearing and the axial fiber stress, (b) the interfacial shearing and the axial fiber stress variation along the load transferring length, (c) the geometrical parameters of the fiber cross-section.

enhance the load-carrying capacity of the composite. This advantage is particularly pronounced in polymer tape-based SPCs, resulting in a synergistic combination of a high fiber volume fraction and an elevated $\gamma$ value, thereby contributing to superior composite performance.

Eq. (7) needs the variation of average interfacial shear with respect to $z$. Assuming a polynomial of the $p$th order in the form:

$$\bar{\tau}_{rz}(z) = \tau_{max}\left(1 - \frac{z}{l_t}\right)^p \tag{9}$$

and integrating Eq. (7), one can obtain the variation of axial stress of the fiber over the transferring length as:

$$\sigma_z^f(z) = \gamma(4/D)\tau_{max}\frac{1-(1-z/l_t)^{p+1}}{(p+1)/l_t} \tag{10}$$

Knowing that the axial stress of fiber reaches its maximum at the end of load transferring length, $\sigma_z^f(l_t) = \sigma_{max}^f$, gives the equation for $l_t$ as:

$$l_t = \frac{D(p+1)\sigma_{max}^f}{4\gamma\tau_{max}} \tag{11}$$

Eq. (10) and Eq. (11) are simplified to the special case of the classical Kelly–Tyson equation by setting a constant value for the interfacial shearing stress, i.e., setting $p = 0$, thus, $\bar{\tau}_{rz}(z) = \tau_{max} = \tau$, and a circular cross-section for the fiber, $\gamma = 1$, resulting in a linear variation for the

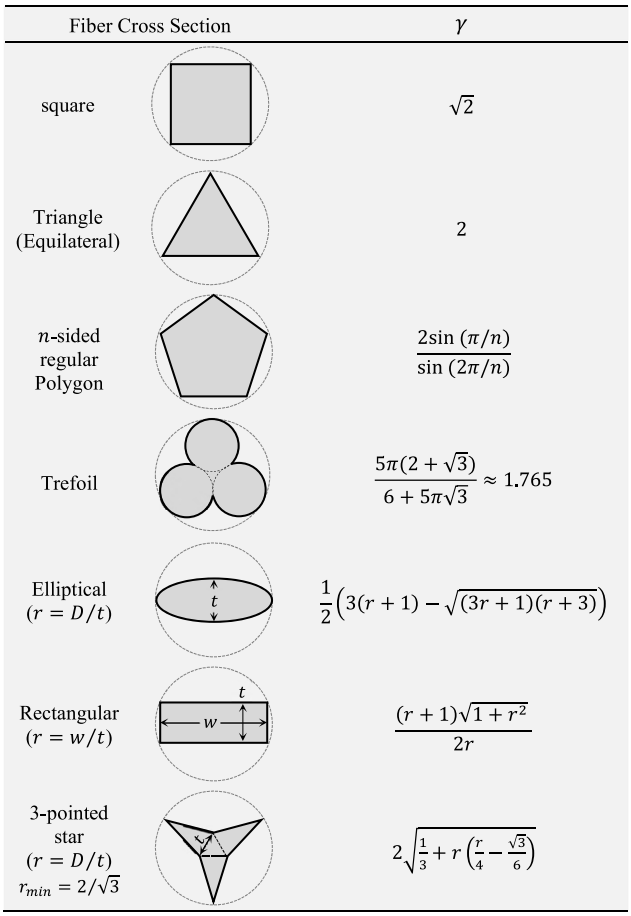


**Fig. 3.** The perimeter-to-area correction factor, $\gamma$, in Eq. (8), for different cross-sections.

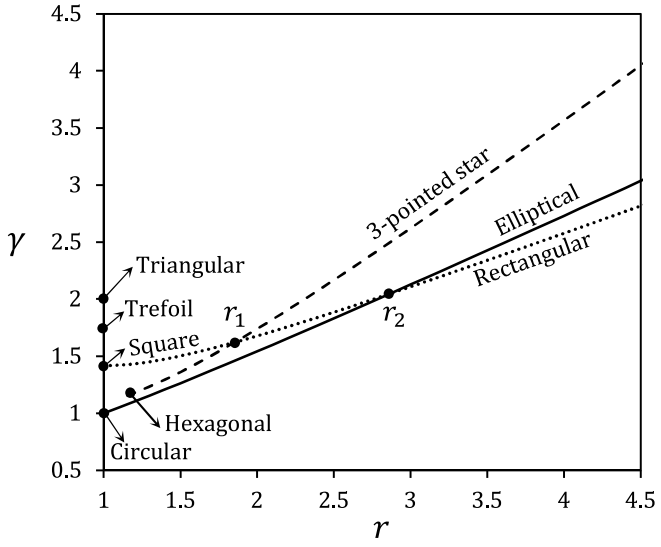


**Fig. 4.** The variation of the cross-section correction factor, $\gamma$, versus geometrical ratio, $r$, defined in Fig. 3.

axial stress of the fiber [37]:

$$\sigma_z^f(z) = \left(\frac{4\tau}{D}\right) z \tag{12}$$

and the load-transferring length of

$$l_t = \frac{D\sigma_{max}^f}{4\tau} \tag{13}$$

Since the axial stress varies along the fiber length, it is useful to obtain the average axial stress, $\bar{\sigma}^f$, carried by a fiber of length $l$ according to the modified shear-lag model. This quantity can be obtained by integrating $\sigma_z^f(z)$ over its length:

$$\bar{\sigma}^f = \frac{1}{l}\int_0^l \sigma_z^f(z)dz \tag{14}$$

Comparing the length of the fiber with the load transferring length, two cases may happen:

*Under Critical Condition*: The length is shorter than twice of transferring length, $l < 2l_t$, which means the fiber is not long enough such that its axial stress reaches the maximum value of $\sigma_{max}^f$ corresponding to $l_t$. The axial stress symmetrically increases from zero starting from both tips and the average stress can be calculated by substituting Eq. (10) to Eq. (14):

$$\bar{\sigma}^f = \frac{2\gamma\tau_{max}}{D}\frac{\left(1-\frac{1}{p+2}\right)}{(p+1)}l \tag{15}$$

which is simplified for the classical Kelly–Tyson equation with $p = 0$, $\tau_{max} = \tau$, and $\gamma = 1$ to:

$$\bar{\sigma}^f = \tau\frac{l}{D} \tag{16}$$

*Over-Critical Condition*: The length is longer than twice of transferring length, $l > 2l_t$, resulting in a length of $l - 2l_t$ at the middle of fiber carrying constant axial stress equal to the maximum value of $\sigma_{max}^f$. Thus, the integral of Eq. (14) is divided into two parts:

$$\bar{\sigma}^f = \frac{1}{l}\left(2\int_0^{l_t}\sigma_z^f(z)dz + (l-2l_t)\,\sigma_{max}^f\right) \tag{17}$$

Replacing $\sigma_z^f(z)$ from Eq. (10) and $l_t$ from Eq. (11) yields:

$$\bar{\sigma}^f = C_1\sigma_{max}^f \tag{18}$$

where

$$C_1 = \left(1 - \frac{2}{(p+2)}\frac{l_t}{l}\right) \tag{19}$$

The coefficient $C_1 < 1$ counts for the effect of the length of discontinuous fibers or the axial stress carried by the transferring length at the tips of a broken continuous fiber and tends to one when $l \gg l_t$. For constant interfacial shearing stress, $p = 0$, Eq. (18) reduces to:

$$\bar{\sigma}^f = \left(1 - \frac{l_t}{l}\right)\sigma_{max}^f \tag{20}$$

Eqs. (18) to (20) reveals that for a specific length of the fiber, $l$, the average stress carried by fiber increases when the load transferring length, $l_t$, decreases. Note that according to Eq. (11), $l_t$ is directly proportional to the outer diameter, $D$, and $(p + 1)$ and is inversely proportional to the cross-section correction factor, $\gamma$, and to the interfacial shear, $\tau_{max}$. The obtained formulation for the average axial stress, $\bar{\sigma}^f$, is used in the next section for estimating the total stress carried by the composite.

### 2.3. The fiber breakage model

In this subsection, the Curtin-statistic fiber breakage model is employed to add the effect of damage progression in fibers to the proposed model. A bundle of continuous fibers is considered, whose strength obeys the Weibull model introduced in Eqs. (4) to (6). The bundle is subjected to axial stress $\sigma(\varepsilon)$, and the fibers break one by one while the axial load increases. When none of the fibers in the bundle has been broken yet, the average stress carried by the fiber bundle is equal to the applied stress. However, as soon as the first fiber breakage happens, the average stress carried by the bundle is reduced, since the broken fiber supports a lower axial load along a length of $2l_t$, (i.e., $\pm l_t$ on both sides of the breaking point) according to the shear-lag analysis. This behavior continues until the average stress of the bundle reaches the ultimate value which corresponds to the breakage of all the fibers in the bundle.

To evaluate the effective average stress of the bundle under applied stress, two factors are needed: the carrying load by a broken fiber with respect to an unbroken fiber, and the fraction of broken fibers. The reduction in the average stress of a broken fiber with respect to an unbroken one, $\hat{C}_1$, can be obtained by setting $l = 2l_t$ in the evaluation of Eq. (19) for the coefficient $C_1$:

$$\hat{C}_1 = 1 - \frac{1}{p+2} \tag{21}$$

which is $\hat{C}_1 = 1/2$ for a constant interfacial shear, $p = 0$, proving the fact that for a linear variation in axial stress, the average equals half, see Eq. (20). On the other hand, the statistical fraction of broken fibers, $\hat{P}$, under the applied stress $\sigma(\varepsilon)$ within a length of $l = 2l_t$ is predicted from Eq. (5) as:

$$\hat{P} = P\left(\sigma(\varepsilon), 2l_t\right) = 1 - exp\left[-\frac{2l_t}{l_0}\left(\frac{\sigma(\varepsilon)}{S_0^f}\right)^{\alpha}\right] \tag{22}$$

where $l_t$ is the load transferring length defined in Eq. (11) corresponding to the maximum stress equal to the applied stress to the bundle, $\sigma_{max} = \sigma(\varepsilon)$. One can rewrite Eq. (22) in a compact form as follows:

$$\hat{P} = 1 - exp\left[-\left(\frac{\sigma(\varepsilon)}{\sigma^*}\right)^{\alpha+1}\right] \tag{23}$$

by introducing the characteristic stress, $\sigma^*$:

$$\sigma^* = \left(\frac{2\left(S_0^f\right)^{\alpha}\gamma\tau_{max}l_0}{D(p+1)}\right)^{\frac{1}{\alpha+1}} \tag{24}$$

The characteristic interfacial shear, $\tau^*_{max}$ is defined as the shear that results in $\sigma^* = S_0^f$ which is calculated by solving Eq. (24) for $\tau_{max}$:

$$\tau^*_{max} = \frac{S_0^f D(p+1)}{2\gamma l_0} \tag{25}$$

Note that Eq. (23) can be approximated by retaining only first-order terms of the exponential function of Taylor series expansion as:

$$\hat{P} \approx \left(\frac{\sigma(\varepsilon)}{\sigma^*}\right)^{\alpha+1} \tag{26}$$

Then, the effective average stress of the fiber bundle, $\bar{\sigma}^f_{eff}$ is:

$$\bar{\sigma}^f_{eff} = \left(1 - \hat{C}_1\hat{P}\right)\sigma(\varepsilon) = C_2\sigma(\varepsilon) \tag{27}$$

where $C_2 = (1 - \hat{C}_1\hat{P})$ is a coefficient that reflects the effect of damage progression in the fibers. Note that $C_2$ is a function of $\sigma(\varepsilon)$ which introduces a softening effect: by increasing $\sigma(\varepsilon)$ until the ultimate applied stress, $\sigma^f_u$, is reached, the last fiber of the bundle breaks and further increments of $\sigma(\varepsilon)$ no longer increases the effective average stress of the bundle. Hence, $\sigma^f_u$ can be taken as the value that makes the variation of $\bar{\sigma}^f_{eff}$ with respect to $\sigma(\varepsilon)$ to zero (horizontal slope in the $\bar{\sigma}^f_{eff} - \sigma(\varepsilon)$ graph). The maximum effective average stress of bundle, $\left(\bar{\sigma}^f_{eff}\right)_u$, is given by equating the derivative to zero:

$$\frac{d(\bar{\sigma}^f_{eff})}{d(\sigma(\varepsilon))} = 0 \tag{28}$$

The approximated Eq. (26) simply gives $\sigma^f_u$ at $\varepsilon = \varepsilon^f_u$ and the corresponding maximum effective strength of bundle:

$$\sigma^f_u \approx \lambda_1(\alpha)\sigma^* \tag{29a}$$

$$\left(\bar{\sigma}^f_{eff}\right)_u \approx \lambda_2(\alpha)\sigma^* \tag{29b}$$

$$\lambda_1(\alpha) = \left(\frac{2}{\alpha+2}\right)^{\frac{1}{\alpha+1}} \tag{29c}$$

$$\lambda_2(\alpha) = \lambda_1(\alpha)\left(1 - \frac{1}{\alpha+2}\right) \tag{29d}$$

However, the exact Eq. (23) yields:

$$\sigma^f_u = h^{\left(\frac{1}{\alpha+1}\right)}\sigma^* \tag{30a}$$

$$\left(\bar{\sigma}^f_{eff}\right)_u = \frac{1}{2}h^{\left(\frac{1}{\alpha+1}\right)}(1 + \exp(-h))\,\sigma^* \tag{30b}$$

at $\varepsilon = \varepsilon^f_u$, where $h$ is the smallest positive root of this equation:

$$1 + (1 - (\alpha+1)h)\exp(-h) = 0 \tag{31}$$

After estimating the strength of the fiber bundle, it is useful to present an approximated expression for the average pull-out length and then the pull-out work as a result of the progressive breakage of fibers which affects the total toughness of the composite. The characteristic length, $\delta^*$, corresponds to the characteristic stress, is introduced as twice the transferring length, $\delta^* = 2l^*$ and is obtained by replacing $\sigma^f_{max}$ with $\sigma^*$ in Eq. (11):

$$\delta^* = \left(\frac{D(p+1)S_0^f(l_0)^{\frac{1}{\alpha}}}{2\gamma\tau_{max}}\right)^{\frac{\alpha}{\alpha+1}} \tag{32}$$

It is shown in [35] that the average pull-out length of fibers, $\langle l_p\rangle$, is proportional to this characteristic length as:

$$\langle l_p\rangle = \frac{1}{4}\lambda_3(\alpha)\delta^* \tag{33a}$$

$$\lambda_3(\alpha) = \left(\frac{0.664}{\alpha^{0.6}} + 0.716\right) \tag{33b}$$

Then, the work per unit area of composite to pull out all of the fibers, $W_p$, is proportional to $\sigma^*\delta^*$ [35]:

$$W_p = \frac{1}{12}\lambda_4(\alpha)v^f\sigma^*\delta^* \tag{34a}$$

$$\lambda_4(\alpha) = \left(\frac{1.87}{\alpha^{0.75}} + 0.50\right) \tag{34b}$$

which is claimed to be accurate (5% approximation) for $m \geqslant 1$ [35]. Substituting Eq. (24) and Eq. (32) into Eq. (34a), yields:

$$W_p = \frac{1}{12}\lambda_4(\alpha)v^f\left(\frac{D(p+1)\left(S_0^f\right)^{\frac{2\alpha}{\alpha-1}}(l_0)^{\frac{2}{\alpha-1}}}{2\gamma\tau_{max}}\right)^{\frac{\alpha-1}{\alpha+1}} \tag{35}$$

Fig. 5 illustrates the variation of $\lambda_1$ to $\lambda_4$ as a function of Weibull modulus in the range of $5 < \alpha < 30$ where the modulus of most of the polymeric fibers stands. The labels $F_i$ correspond to the PA6 fibers experimentally investigated in Section 3.

The extra absorbed energy by the composite is equivalent to the pull-out work which enhances the toughness of the composite. $W_p$ can be converted to the strain energy per unit volume, i.e., the area under the stress–strain curve by dividing it by the gauge length of the composite sample under axial loading, $L$:

$$T_p = \frac{W_p}{L} \tag{36}$$

To add an approximated horizontal pull-out line at the end of the stress–strain curve, it is assumed that the total extra pull-out strain, $\bar{\varepsilon}_p$, is:

$$\bar{\varepsilon}_p = \frac{\langle l_p\rangle}{L} \tag{37}$$

and the average pull-out stress, $\bar{\sigma}_p$, can be estimated as:

$$\bar{\sigma}_p = \frac{W_p}{\langle l_p\rangle} \tag{38}$$

The total toughness of the composite is obtained by adding Eq. (36) to the general $N$-segmented expression for the toughness presented in Eq. (3).

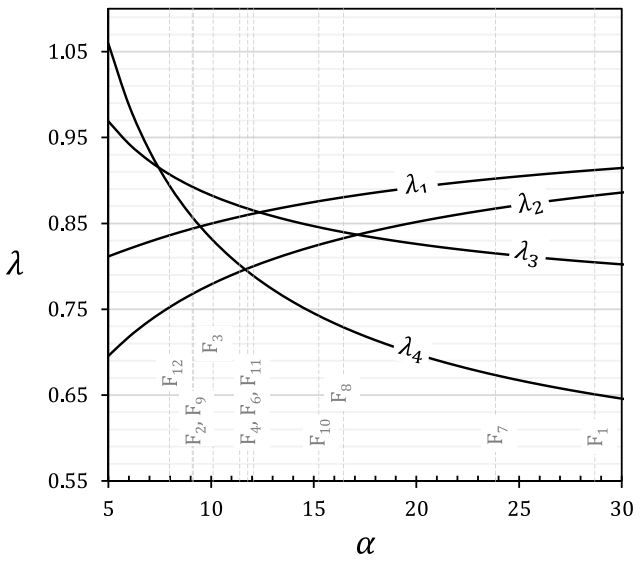


**Fig. 5.** Variation of $\lambda_i$ parameters with respect to $\alpha$.

### 2.4. The progressive micromechanics model

The progressive micromechanics model for composites under longitudinal tensile loading can be established on the basis of volume averaging of axial stresses on the components. In fact, the proposed model is a modified version of the standard rule-of-mixture benefiting the modified shear-lag analysis, and the fiber breakage model presented in Section 2.2 and Section 2.3, respectively. Given the approximated $N$-segmented representative stress–strain curves for the fibers and the matrix introduced in Eq. (1), the progressive model aims to predict the corresponding $N$-segmented stress–strain curve of the composite. Then, the strength, $S_c$, and the toughness, $T_c$, of the composite can be achieved from Eqs. (2) and (3) with the additional term of pull-out introduced in Eq. (36).

The equilibrium in a random cross-section perpendicular to the direction of fibers, which are aligned parallel to the applied tensile strain, $\varepsilon$, yields the relationship between the equivalent axial stress of the composite, $\bar{\sigma^c}(\varepsilon)$, and the effective average stress carried by the fibers, $\bar{\bar{\sigma}}^f(\varepsilon)$, and the matrix, $\bar{\sigma}^m(\varepsilon)$, as:

$$\bar{\sigma^c}(\varepsilon) = v^f \bar{\bar{\sigma}}^f(\varepsilon) + \left(1 - v_f\right) \bar{\sigma}^m(\varepsilon) \tag{39}$$

For the matrix, it is assumed that the average axial stress carried in every cross-section is the same and can be captured from the stress corresponding to the applied strain, $\varepsilon$, from its stress–strain curve, $\bar{\sigma}^m(\varepsilon) = \sigma^m(\varepsilon)$. For determining the effective average stress of the fibers in the cross-section, first of all, the fiber length, $l$, should be compared to a critical length to determine if the fiber is in *Under* or *Over* critical condition. The critical length, $l_c$, is twice the transferring length, $l_t$, defined in Eq. (11), however, by setting the maximum stress equal to the reference strength of fiber, $\sigma^f_{max} = S^f_0$:

$$l_c = \frac{D\,(p+1)\,S^f_0}{2\gamma\tau_{max}} \tag{40}$$

Note that this comparison is valid for discontinuous fibers and it is meaningless for continuous fibers which are always subjected to *Over* critical condition since the length is assumed to be infinity, $l \to \infty$. Two cases may occur:

*Case one,* $l < l_c$: According to *Under* Critical Conditions in Section 2.2, the average stress carried by the fibers is obtained from Eq. (15), resulting in a weak strengthening effect. The average stress of the composite is obtained from Eq. (39) by replacing $\bar{\bar{\sigma}}^f$ with Eq. (15):

$$\bar{\sigma^c}(\varepsilon) = 2\gamma\tau_{max}\frac{l}{D}\frac{\left(1 - \frac{1}{p+2}\right)}{(p+1)} v^f + \left(1 - v_f\right)\sigma^m(\varepsilon) \tag{41}$$

In Eq. (41), it is assumed that the interfacial shearing stress slightly and linearly increases by increasing the applied strain to reach its maximum capacity. Since for $l < l_c$ the stress in the fiber never reaches $S^f_0$, it is expected that the composite fails when the applied strain reaches the failure strain of the matrix, $\varepsilon = e^m$, and its corresponding strength, $S^m = \sigma^m(e_m)$. Thus, the strength of the composite, $S^c$, can be obtained from Eq. (41) by replacing $\sigma^m(\varepsilon)$ with $S^m$:

$$S^c = 2\gamma\tau_{max}\frac{l}{D}\frac{\left(1 - \frac{1}{p+2}\right)}{(p+1)} v^f + \left(1 - v_f\right) S^m \tag{42}$$

Note that the contribution of these short fibers is only in terms of interfacial shearing stress and it is independent of the properties of fibers. It is why interfacial strength is vital for strengthening with low-sized reinforcements, $l \ll l_c$, e.g., nanocomposites.

*Case two,* $l > l_c$: In this case, the fibers are long enough to present an effective reinforcement, however, $\sigma^f(\varepsilon)$ captured directly from the fiber stress–strain curve, should be modified by two correction factors, $C_1$, and $C_2$ to take into account the reduction of load carrying along the transferring length and the progressive breakage of fibers, respectively discussed in Section 2.2 (Eq. (19)) and Section 2.3 (Eq. (27)). It is obvious that for continuous fibers, where theoretically $l \to \infty$, the coefficient $C_1 \to 1$, and for the fibers with completely uniform properties, where theoretically $\alpha \to \infty$, the coefficient $C_2 \to 1$.

In addition to $C_1$ and $C_2$, a third correction factor, $C_3$, is defined, to take into account the size-dependent strength of the composite as a result of the size-dependent strength of fibers defined in Eq. (6):

$$C_3 = \left(\frac{l_0}{l}\right)^{1/\alpha'} \tag{43}$$

in which $\alpha'$ is a fitting parameter, used for calibrating the numerical simulations and/or experimental measurements on the properties of composites of different sizes. It is reported in many cases of studies [35] that the sensitivity of the composite to the size effect is less than that of the fiber meaning that $\alpha' > \alpha$. Note that not only the length of the fiber, $l$, but also the number of fibers may represent the size-dependency, which is not covered here. Applying all the considered corrections, the average effective stress carried by the fibers, $\bar{\bar{\sigma}}^f(\varepsilon)$, and then the average stress of composite, $\bar{\sigma}_c(\varepsilon)$ is estimated as:

$$\bar{\bar{\sigma}}^f(\varepsilon) = C_1 C_2 C_3 \sigma^f(\varepsilon) \tag{44a}$$

$$\bar{\sigma}^c(\varepsilon) = v^f C_1 C_2 C_3 \sigma^f(\varepsilon) + \left(1 - v_f\right)\sigma^m(\varepsilon) \tag{44b}$$

where $C_1$, as a function of applied strain, $\varepsilon$, is replaced from Eqs. (11) and (19) with $\sigma^f_{max} = \sigma^f(\varepsilon)$. Unlike *Under* critical condition where the failure of the composite is always corresponding to the failure of the matrix, for *Over* critical condition two different scenarios for the failure of the composite are conceivable depending on which one of the fiber or the matrix reaches its failure strain sooner.

*Scenario one,* $e^m > \varepsilon^f_u$:

In this scenario the fibers are completely broken at the strain, $\varepsilon = \varepsilon^f_u$, defined in Eq. (29a) or Eq. (30a), however, the matrix has not reached its failure strain, $e^m$, yet. The maximum effective stress carried by the fibers just before all the fibers are broken can be obtained from Eq. (44a) by replacing $C_2\sigma^f(\varepsilon)$ with $\left(\bar{\sigma}^f_{eff}\right)_u$ according to Eq. (27):

$$\bar{\bar{\sigma}}^f\left(\varepsilon^f_u\right) = C_1 C_3 \left(\bar{\sigma}^f_{eff}\right)_u \tag{45}$$

Thus, assuming that failure of the composite corresponds to the failure of the fibers, $e^c = \varepsilon^f_u$, one can estimate the strength of the composite by inserting Eq. (45) into Eq. (44b):

$$S^c = v^f C_1 C_3 \left(\bar{\sigma}^f_{eff}\right)_u + \left(1 - v^f\right)\sigma^m\left(\varepsilon^f_u\right) \tag{46}$$

where $\sigma^m(\varepsilon^f_u) \leqslant S^m$ is the stress carried by the matrix at $\varepsilon^f_u$ evaluated from its stress–strain curve. The assumption that the composite fails

when the fibers fail, $e^c = \varepsilon_u^f$, is correct if the complete breakage of fibers results in the sudden failure of the matrix. It needs:

$$S^c > \left(1 - v^f\right) S^m \tag{47}$$

since whole the composite load should be carried by the matrix in the absence of the fibers. Substituting Eq. (46) into Eq. (47), determines a minimum volume fraction for the fibers, $v_{min}^f$, that must be exceeded if the strength of the composite, $S_c$, is to be given by Eq. (46):

$$v_{min}^f = \frac{S^m - \sigma^m(\varepsilon_u^f)}{C_1 C_3 \left(\overline{\sigma}_{eff}^f\right)_u + S^m - \sigma^m(\varepsilon_u^f)} \tag{48}$$

where $C_1$ is obtained from Eq. (11) and Eq. (19) with $\sigma_{max}^f = \sigma_u^f$. Otherwise, when $v^f < v_{min}^f$, the applied strain should be increased progressively to reach the maximum elongation of the matrix which is indeed the elongation of the composite, $e_c = e^m$, and the strength of the composite is:

$$(S^c)' = (1 - v^f)\sigma^m(\varepsilon_u^f) \quad \text{for} \quad v^f < v_{min}^f \tag{49}$$

Of course, it is not a desirable reinforcing condition since the fibers act like voids in the matrix. In addition, it is useful to check if laying fibers in the matrix results in any reinforcing effect by comparing the strength of the composite to the strength of the matrix before composition with the fibers. Equating Eq. (46) to $S^m$ defines a critical volume fraction of the fibers, $v_{cr}^f$ as:

$$v_{cr}^f = \frac{S^m - \sigma^m(\varepsilon_u^f)}{C_1 C_3 \left(\overline{\sigma}_{eff}^f\right)_u - \sigma^m(\varepsilon_u^f)} \tag{50}$$

One can see from Eq. (48) and Eq. (50) that always $v_{min}^f < v_{cr}^f$ which means the condition $v^f > v_{cr}^f$ always automatically satisfies $v^f > v_{min}^f$ [37].

*Scenario two*, $e^m < \varepsilon_u^f$:

In this scenario, the matrix failure happens before the complete breakage of the fibers. The average stress in the composite is evaluated by Eq. (44) and it is assumed that the composite fails when the matrix fails, i.e., $e^c = e^m$. Thus, the strength of the composite is evaluated from Eq. (44b) at $\varepsilon = e^m$:

$$S^c = v^f C_1 C_2 C_3 \sigma^f(e^m) + \left(1 - v_f\right) S^m \tag{51}$$

where $\sigma^f(e^m)$ is the partial contribution of the fiber in the maximum carried stress by the composite. Note that according to this scenario when the matrix fails at the strains much lower than that of fibers, a significant loss in reinforcing potential of the fibers may happen as a result of anticipating the composite failure. Hence, the majority of commercial PPC/SPCs are designed in such a way that this scenario is improbable due to the fact that the isotropic matrix typically exhibits a considerably higher strain to failure compared to the fibers.

After a clear definition of the failure scenarios, the proposed progressive model is ready to be applied for the prediction of the stress–strain curve of the composite: the applied strain increases from $\varepsilon = 0$ by an increment of $\Delta\varepsilon$. The stresses carried by the components, $\sigma^f(\varepsilon)$ and $\sigma^m(\varepsilon)$, are evaluated from their $N$-segmented stress–strain curves introduced in Eq. (1). The corresponding average stress of composite is calculated according to the *Under* or *Over* critical conditions. The tangent modulus of composite, $E_c(\varepsilon)$, as the slope of its stress–strain curve is calculated as:

$$E^c(\varepsilon) = \frac{\sigma^c(\varepsilon + \Delta\varepsilon) - \sigma^c(\varepsilon)}{\Delta\varepsilon} \tag{52}$$

Increasing the applied strain continues to reach the failure strain of the composite, $\varepsilon = e^c$ which is defined by the failure scenario to find the strength of the composite, $S^c$. Finally, the toughness can be estimated as the area under the generated stress–strain curve of composite using Eq. (3) by adding the pull-out term presented in Eq. (36).

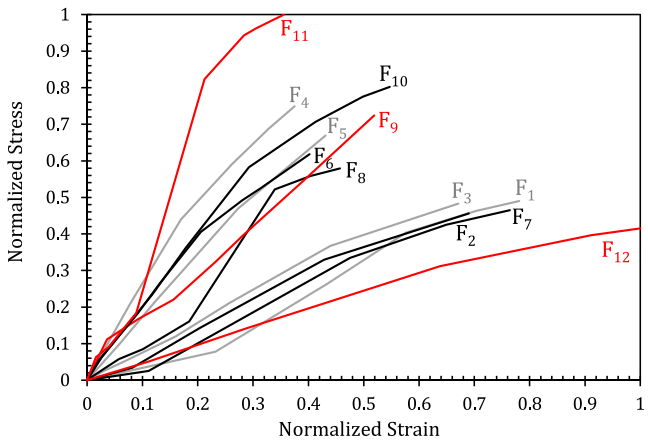


**Fig. 6.** The normalized $N$-segmented stress–strain curves of the PA6 fibers, $F_1$ to $F_{12}$.

## 3. Experimental measurements for the inputs of the model

In this section, the experimental measurements of the required inputs for the proposed progressive model are presented and analyzed. Both the reinforcing fiber and the matrix are assumed to be made of PA6 polymer. 12 different PA6 fibers, named $F_1$ to $F_{12}$, having a variety of cross-section sizes and shapes listed in Table 1 are tested by a tensile test machine. For the fibers, $F_1$ to $F_8$ the number of repetitions is limited to 5, while for $F_9$ to $F_{12}$ adequate samples are tested to guarantee the accuracy in the evaluation of statistical Weibull parameters since these fibers are used for more detailed studies on the properties of PA6-based SPCs. For the matrix, 10 different anionic PA6, named $M_1$ to $M_{10}$, with a wide range of elongations at the break due to various types of raw materials as well as different types and dosages of additives are considered for tensile tests. It provides 120 different combinations of fibers and matrices as a huge design space for fabricating PA6-based SPCs.

First of all, a systematic approach for post-processing of the stress–strain curves obtained from experiments is needed to make them suitable for insertion into the model by converting them to an $N$-segmented version compatible with Eq. (1). The step-by-step procedure for this approximation is explained in Appendix in detail. The approximated $N$-segmented stress–strain curves for the PA6 fibers and matrices are plotted in Fig. 6 and Fig. 7, respectively. All the stresses are normalized to the strength of the strongest Fiber, $F_{11}$, while all the strains are normalized to the elongation at the break of the most flexible fiber, $F_{12}$, denoted by $\check{(.)}$ superscript:

$$\check{\sigma} = \frac{\sigma}{(S^f)_{F_{11}}}, \check{\varepsilon} = \frac{\varepsilon}{(e^f)_{F_{12}}} \tag{53}$$

The normalized mean strength, $\check{S} = S/(S^f)_{F_{11}}$, and failure strain, $\check{e} = e/(e^f)_{F_{12}}$, of the fibers and the matrices are presented in Table 1.

Then, the Weibull parameters of the fibers are extracted from the experiments. From Eq. (5), the cumulative probability of fiber failure at the measured stress $S^f$ is:

$$P\left(S^f\right) = 1 - exp\left[-\left(\frac{S^f}{S_0^f}\right)^{\alpha}\right] \tag{54}$$

Note that the length of fiber samples under tensile test is indeed the reference length, i.e., $l = l_0$, which is substituted in Eq. (5). Rearranging and taking the natural logarithm of both sides of Eq. (54), one can obtain the following representation:

$$\ln\left(\ln\left(\frac{1}{1-P}\right)\right) = \alpha \ln S^f - \alpha \ln S_0^f \tag{55}$$

To evaluate the Weibull parameters from experiments, first, the measured strengths of $n$ fiber samples are ranked in ascending order,

**Table 1**
Geometry and normalized properties of the PA6 fiber, $F_1$ to $F_{12}$.

| Fiber | No. samples | $l_0$ [mm] | $\tau^*/\tau^*_{(F_{11})}$ | Cross section | | Weibull | | Means | |
|---|---|---|---|---|---|---|---|---|---|
| | | | | $D$ [μm] | $\gamma$ | $\check{S}_0^f$ | $\alpha$ | $\check{e}$ | $\check{S}$ |
| $F_1$ | 5 | 10 | 1.165 | 71 | 1.97 | 0.478 | 28.69 | 0.781 | 0.490 |
| $F_2$ | 5 | 10 | 0.833 | 72 | 2.69 | 0.460 | 9.13 | 0.690 | 0.456 |
| $F_3$ | 5 | 10 | 0.885 | 55 | 2.04 | 0.486 | 10.10 | 0.671 | 0.483 |
| $F_4$ | 5 | 10 | 0.555 | 11 | 1 | 0.746 | 12.08 | 0.375 | 0.749 |
| $F_5$ | 5 | 10 | 0.961 | 22 | 1 | 0.647 | 54.34 | 0.431 | 0.669 |
| $F_6$ | 5 | 10 | 0.498 | 21 | 1.76 | 0.617 | 11.40 | 0.402 | 0.618 |
| $F_7$ | 5 | 10 | 1.145 | 75 | 2.03 | 0.459 | 23.86 | 0.764 | 0.465 |
| $F_8$ | 5 | 10 | 0.766 | 50 | 2.52 | 0.571 | 16.46 | 0.457 | 0.579 |
| $F_9$ | 41 | 20 | 8.495 | 343 | 1 | 0.733 | 9.08 | 0.519 | 0.724 |
| $F_{10}$ | 26 | 20 | 1.677 | 62 | 1 | 0.795 | 15.25 | 0.547 | 0.802 |
| $F_{11}$ | 23 | 20 | 1 | 28 | 1 | 1 | 11.79 | 0.356 | 1 |
| $F_{12}$ | 18 | 20 | 0.199 | 55 | 3.79 | 0.406 | 7.97 | 1 | 0.415 |
| $M_1$ | 5 | – | – | – | – | – | – | 0.065 | 0.082 |
| $M_2$ | 5 | – | – | – | – | – | – | 0.572 | 0.087 |
| $M_3$ | 5 | – | – | – | – | – | – | 0.200 | 0.097 |
| $M_4$ | 5 | – | – | – | – | – | – | 0.252 | 0.087 |
| $M_5$ | 5 | – | – | – | – | – | – | 0.101 | 0.028 |
| $M_6$ | 5 | – | – | – | – | – | – | 0.114 | 0.101 |
| $M_7$ | 5 | – | – | – | – | – | – | 0.512 | 0.099 |
| $M_8$ | 5 | – | – | – | – | – | – | 0.605 | 0.092 |
| $M_9$ | 5 | – | – | – | – | – | – | 0.244 | 0.081 |
| $M_{10}$ | 5 | – | – | – | – | – | – | 0.090 | 0.088 |

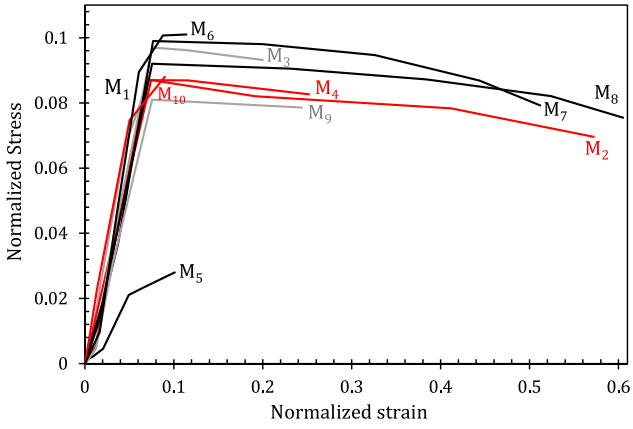


**Fig. 7.** The normalized $N$-segmented stress–strain curves of the PA6 matrices, $M_1$ to $M_{10}$.

$i = 1, 2, \ldots, n$. Then, the ordered probabilities corresponding to the $i$th measured strength in the ranking can be calculated as:

$$P_i = \left(\frac{i - 0.5}{n}\right) \tag{56}$$

Replacing the ranked strengths, $S_i^f$, and the corresponding probabilities, $P_i$, into the right hand and the left hand of Eq. (55) provides the pair coordinates of $n$ points:

$$\ln\left(\ln\left(\frac{1}{1-P_i}\right)\right) = \alpha \ln S_i^f - \alpha \ln S_0^f \tag{57}$$

By a linear curve fitting of Eq. (55) among the points obtained from Eq. (57), one can evaluate the reference strength, $S_0^f$, and the Weibull modulus, $\alpha$, from the interpolated slope and intercept. The calculated Weibull moduli as well as the reference strengths which are normalized to the reference strength of fiber $F_{11}$, i.e., $\check{S}_0^f = S_0^f/(S_0^f)_{F_{11}}$, are listed in Table 1 for all the tested fibers.

## 4. Results and discussion

In this section, the progressive micromechanics model proposed in Section 2 is employed to predict the properties of PA6-based SPCs. The required inputs of the model are presented in Section 3 from an enormous set of experimental measurements on available PA6 fibers and matrices with a wide range of geometrical and mechanical properties. As seen in Table 1, for all the fibers, the required properties, i.e., diameter, $D$, cross-section correction factor, $\gamma$, reference length, $l_0$, reference strength, $S_0^f$, and the Weibull modulus, $\alpha$, are given. The fitting parameter for the size effect, $\alpha'$, defined in Eq. (43), is assumed to be equal to the Weibull modulus, $\alpha' = \alpha$, due to the lack of experimental data. In addition, the approximated $N$-segmented stress–strain curves of the fibers are provided in Table A.1. On the other hand, the mean strength and mean failure strain of the matrices listed in Table 1 in conjunction with the approximated $N$-segmented stress–strain curves of the fibers provided in Table A.2, fully define the required properties of the matrix for the model. Note that for the purpose of generality, all the reported stresses and strains are normalized according to Eq. (53).

Reviewing the model development from Eq. (1) to Eq. (52), one can see that the only inputs remaining to be defined are the power, $p$, and the maximum interfacial shear, $\tau_{max}$. The power, $p$, was introduced in Eq. (9) to consider the general assumption of non-constant interfacial shear with the maximum, $\tau_{max}$, at the tip of the fibers. Although the progressive micromechanics model has the ability to capture this shearing stress concentration at the tip of the fibers breakages with $p \neq 0$, however, for the presented results a constant interfacial shearing stress is assumed, resulting in $p = 0$ and $\tau_{max} \to \tau$. In other words, the classical Kelly–Tyson equation for interfacial shear with linear variation in axial stress along the fiber is applied for these numerical results. This averaged-sense interfacial shear is the key parameter in the prediction of the properties of the PA6-based SPCs. In order to perform a parametric study, first, the characteristic interfacial shear stress, $\tau^*$, of the fiber with the highest strength, $F_{11}$, is calculated by Eq. (25) and the interfacial shear, $\tau$ is normalized to it as:

$$\check{\tau} = \frac{\tau}{\tau^*_{(F_{11})}} \tag{58}$$

Then, a range of variations for the interfacial shear stress is assumed:

$$0.1 < \check{\tau} < 5 \quad \text{or} \quad 0.1\tau^*_{(F_{11})} < \tau < 5\tau^*_{(F_{11})} \tag{59}$$

For the fiber $F_{11}$ itself, it is a reasonable range from a weak (10% of its characteristic) to a strong (500% of its characteristic) bonding. However, one needs to compare the characteristic interfacial shear stress of the other fibers to $\tau^*_{(F_{11})}$ to have an idea about the mapping of the selected range for them. The ratio of characteristic interfacial shear

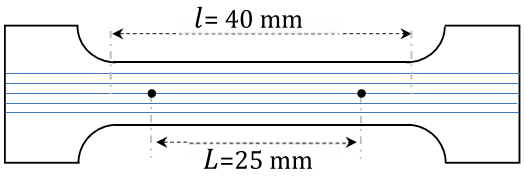


**Fig. 8.** The schematic of the PA6 SPC samples under tensile test. The length of the fibers outside the grips is $l$ and assumed to be 40 mm and the gauge length, $L$, for recording displacement and converting to the strain is assumed to be 25 mm.

stress for all the fibers is listed in Table 1. When $\tau^*_{(F_i)}/\tau^*_{(F_{11})} < 1$, the selected range of interfacial shear stress results in stronger bonding with respect to the characteristic shear stress. For example, from Table 1 it can be obtained that $\tau^*_{(F_{11})} \approx 5\tau^*_{(F_{12})}$. Substituting into the selected range in Eq. (59), the interfacial shear stress, $\tau$, for $F_{12}$, varies from 50% to 2500% of its characteristic value. In contrast, for $\tau^*_{(F_i)}/\tau^*_{(F_{11})} > 1$, the selected range is mapped to relatively weaker bonding compared to the characteristic shear stress. For instance, fiber $F_9$ presents the highest characteristic shear, $\tau^*_{(F_{11})} \approx 0.118\tau^*_{(F_9)}$ resulting a low range of interfacial shear stress from 1.18% to 59% of its characteristic shear stress. In other words, for an identical interfacial shear stress, $\tau$, $F_{12}$ has the strongest bonding while $F_9$ presents the weakest one. The reason is in definition and physical meaning of $\tau^*$ in Eq. (25) which is proportional to the diameter, $D$, and inversely proportional to the $\gamma$ correction factor. Note that $F_9$ has the maximum $D$ and minimum $\gamma$ while $F_{12}$ is vise-versa. It makes sense physically that a fiber with a thicker diameter and circular cross-section provides the lowest bonding since both reduce the interacting surface between the fiber and the matrix. In the upcoming parametric study, the focus is on these three fibers as the main representatives of the PA6 fibers: $F_9$, the thickest with the lowest interaction surface, $F_{11}$, the strongest, and $F_{12}$, with the maximum failure strain.

In order to assess the model and predict the stress–strain curve of the SPC samples under unidirectional loading, the length of continuous PA6 fibers outside the grips of the tensile test machine is assumed to be $l$ = 40 mm, and the gauge length of the sample for recording displacement and converting to the strain is selected to be $L$ = 25 mm, as schematically shown in Fig. 8. This dimension imposes an upper limit for the average pull-out length, $\langle l_p \rangle$ introduced in Eq. (33), as it cannot increase indefinitely even for very low interfacial shear stress. Here, the upper limit for the average pull-out length of the fibers is assumed to be 25% of the total fiber length,i.e., $\langle l_p \rangle_{max} = 0.25\ l = 10$ mm.

Fig. 9 plots the critical length introduced in Eq. (40), normalized to the fiber length, $l_c/l$, versus the normalized interfacial shear, $\check{\tau}$, for the fibers $F_9$, $F_{11}$, and $F_{12}$. It is seen that fiber $F_{12}$ which presents the maximum potential of bonding with the matrix thanks to its non-circular cross-section, has the lowest critical length, always in the desirable over-critical zone ($l_c/l < 1$), even for a very low interfacial shear stress. In contrast, $F_9$ provides the highest critical length with an exponential increase for low interfacial shear stresses, $\check{\tau} < 1$, resulting in an under-critical condition. Only for high enough interfacial shear stresses, $\check{\tau} > 4.3$, it drops to over-critical condition. Fiber $F_{11}$ behaves more similar to $F_{12}$, however, proposes a higher critical length because it is the strongest fiber, notice $S_0^f$ in the numerator of Eq. (40), and it has a circular cross-section with $\gamma = 1$. However, $F_{11}$ rapidly reaches the desirable over-critical condition for $\check{\tau} > 0.5$. The same trend is observed for characteristic length, $\delta^*$, defined in Eq. (32). It is used to evaluate the average pull-out length which is investigated in Fig. 10.

The variation of the average pull-out length normalized to the fiber length, $\langle l_p \rangle/l$, with respect to the normalized interfacial shear stress, $\check{\tau}$, for the fibers $F_9$, $F_{11}$, and $F_{12}$ is demonstrated in Fig. 10. In general, increasing the interfacial shear stress decreases the average pull-out length, as expected due to the strengthening of the bonding between the fiber and the matrix and in other words the lower critical length.

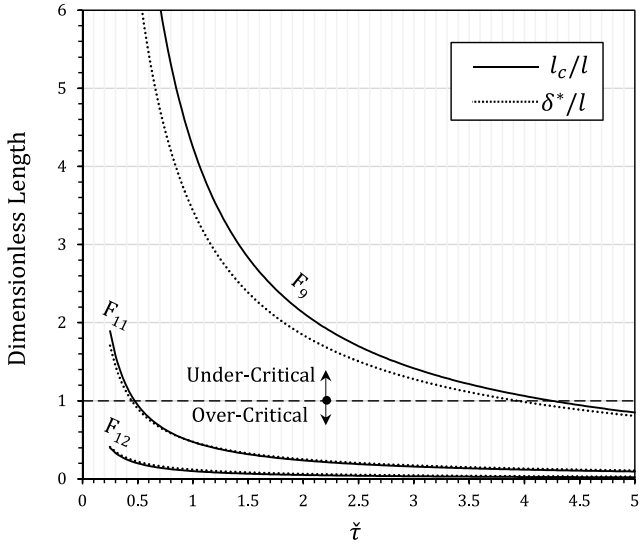


**Fig. 9.** Variation of the normalized critical length $l_c/l$ and the normalized characteristic length, $\delta^*/l$, with respect to the normalized interfacial shear stress, $\check{\tau}$, for the selected PA6 fibers, $F_9$, $F_{11}$, and $F_{12}$. The length of fibers is set to $l$ = 40 mm.

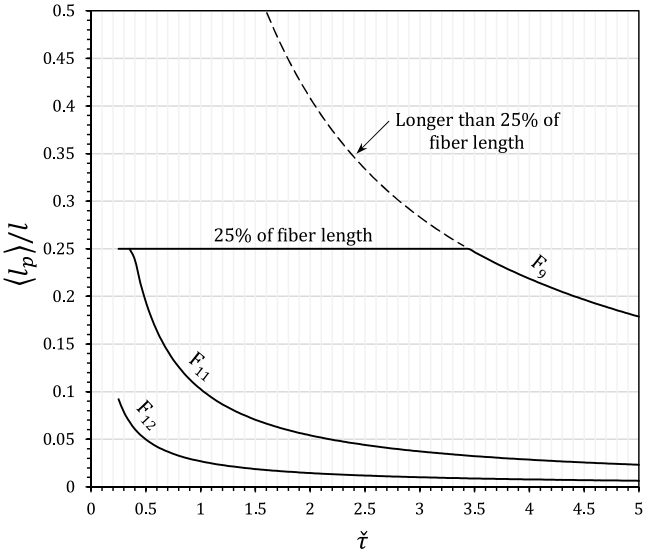


**Fig. 10.** Variation of the normalized average pull-out length, $\langle l_p \rangle/l$ with respect to the normalized interfacial shear stress, $\check{\tau}$, for the selected PA6 fibers, $F_9$, $F_{11}$, and $F_{12}$. The length of fibers is set to $l$ = 40 mm.

One observes that around $\check{\tau} = 3.5$ fiber $F_9$ reaches the upper limit of the average pull-out length (which is assumed to be 25% of fiber length) imposed by the total length of the fiber within the SPC sample, see Fig. 8. For $\check{\tau} < 3.5$ fiber $F_9$ is capable of providing even longer average pull-out lengths if the SPC sample is longer as well, plotted by dashed-line. Fiber $F_{12}$ gives the shortest pull-out length, less than 10% of the fiber length even for very low interfacial shear stresses as a result of its non-circular cross-section, lower strength compared to $F_{11}$. Fiber $F_{11}$ approaches the upper limit for the normalized interfacial shear stress as low as $\check{\tau} = 0.5$.

Fig. 11 compares fibers $F_9$, $F_{11}$, and $F_{12}$ in terms of the effect of interfacial shear stress, $\check{\tau}$, on the characteristic normal stress, defined in Eq. (24). $\sigma^*$ has been normalized to the strength of $F_{11}$, i.e., $\check{\sigma}^* = \sigma^*/(S_0^f)_{F_{11}}$. The characteristic normal stress is used by the model for evaluating both the effective strength of the fiber bundle, defined in Eq. (29b), and the pull-out work, defined in Eq. (34a). The general

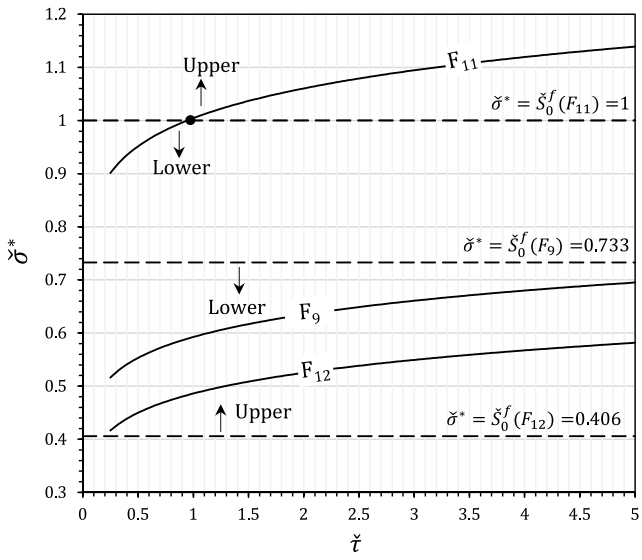


**Fig. 11.** Variation of the normalized characteristic stress of the fiber bundles, $\check{\sigma}^*$, with respect to the normalized interfacial shear, $\check{\tau}$, for the selected PA6 fibers, $F_9$, $F_{11}$, and $F_{12}$.

trend of $\check{\sigma}^*$ versus $\check{\tau}$ is increasing for all the fibers which means the higher the interfacial shear stress the higher the strength of the fiber bundle under progressive breakage. However, it is not correct to conclude in the same way that increasing $\check{\tau}$ results in an increase in put-out work because according to Eq. (34a) the pull-out work is proportional to $\sigma^*\delta^*$, and as seen before in Fig. 9, $\delta^*$ decreases. It is seen that for the plotted range of normalized interfacial shear stress, $\check{\sigma}^*$ of $F_{12}$ is always higher than its normalized reference strength, $(S_0^f)_{F_{12}} = 0.406$ (see Table 1), while, for $F_9$ it is always lower than its normalized reference strength, $(S_0^f)_{F_9} = 0.733$. The behavior of fiber $F_{11}$ is between, where it is lower than $(S_0^f)_{F_{11}} = 1$ for $\check{\tau} < 1$ and is higher afterward. The observed influence of interfacial shear stress on the effective strength of fiber bundles can significantly affect the predicted properties of SPC as will be presented in upcoming results. Note that a reduction in the effective strength of the bundle will also result in a reduction in its failure strain of the fiber bundle, see Section 2.3, which is vital when compared to the failure strain of the matrix to predict the failure scenario of SPC as explained in Section 2.4.

Fig. 12(a) to (c) respectively demonstrate the normalized stress–strain curve of the fiber bundles, $F_9$, $F_{11}$, $F_{12}$ for three different normalized interfacial shear stresses, $\check{\tau} = 0.1$, 1, 5 according to Eq. (27). As seen, when $\check{\tau}$ decreases, the complete breakages of the fiber bundle happens sooner resulting in lower effective strength, $\left(\bar{\sigma}_{eff}^f\right)_u$, as well as lower failure strain, $e_u^f$, due to its statistical nature explained by the Weibull model. It is obvious that a reduction in the effective strength of the bundle reduces the strength of SPC as well, however, one should notice the reduction in the failure strain of the bundle, $e_u^f$, with more scrupulosity, since it defines the failure scenario of SPC when compared to the failure strain of the matrix, $e^m$. Probing the failure stain of the matrices in Fig. 7, the matrices can be categorized into three groups: brittle group with $\check{e} < 0.12$, i.e., $M_1$, $M_5$, $M_6$, and $M_{10}$, intermediate group with $0.12 < \check{e} < 0.25$, i,e., $M_3$, $M_4$, and $M_9$, and tough group with $0.25 < \check{e} < 0.61$, i.e., $M_2$, $M_7$, and $M_8$. For the purpose of clarity in the presented graphs, matrices $M_{10}$, $M_4$, and $M_2$ are selected as the representative of brittle, intermediate, and tough groups, respectively, which are plotted in red in Fig. 7. From Fig. 12(a) it is seen that for the fiber $F_9$ with the mean failure strain, $\check{e}^f = 0.519$, the failure strain of fiber bundle is higher than the brittle and the intermediate matrices while it is lower than the tough group in the range of interfacial shear stress, $0.1 < \check{\tau} < 5$. The failure strain of the bundle of fiber $F_{11}$ is higher than the brittle group and lower than the tough group. However, since its mean failure strain, $\check{e}^f = 0.356$, is in the range of the failure strain of intermediate matrices, variation in the interfacial shear stress can shift its failure strain between $e_u^f < e^m$ and $e_u^f > e^m$ which means that the failure scenario is changed by modifying the interfacial shear stress. Since the fiber $F_{12}$ is the most ductile one, the failure strain of its bundle is higher than all the matrix groups even for a low interfacial shearing stress.

The normalized stress–strain curves predicted by the progressive micromechanics model for the PA6-based SPCs composed of the Fiber $F_9$ with the volume fraction, $v^f = 0.15$, and three different interfacial shearing stresses are presented in Fig. 13 where the matrix is assumed to be brittle ($M_{10}$), intermediate ($M_4$), or tough ($M_2$), in Fig. 13(a), (b), or (c), respectively. As shown before in Fig. 9 and Fig. 11, even the normalized interfacial shear stress, $\check{\tau} = 5$, is a relatively weak bonding for the fiber $F_9$ due to its high strength and thick circular cross-section. Hence, a high enough interfacial shear stress of $\check{\tau} = 50$ is assumed for this fiber to also demonstrate a strong bonding with a low pull-out phenomenon. In accordance with Fig. 12(a), for both $M_{10}$ and $M_4$ matrices the failure of SPC is based on scenario 2 since $e^m < e_u^f$, while for the tough matrix, $M_2$, it switches to scenario 1 because the failure strain of fiber remains lower than that of the matrix even for a high interfacial shear stress of $\check{\tau} = 50$ which makes possible to take the full advantage of fiber in terms of strengthening. It is observed that for low values of interfacial shear a long horizontal line is added to the stress–strain curve corresponding to a long average pull-out length as shown in Fig. 10 for $F_9$.

Fig. 14 illustrates the normalized stress–strain curves for the SPCs composed of the strongest fiber, i.e., $F_{11}$ with the volume fraction, $v^f = 0.15$ for $M_{10}$, $M_4$, or $M_2$ matrices. Three different interfacial shear stresses, $\check{\tau} = 0.1$, 1, and 5 are assumed for every matrix to see the effect of bonding on the properties of the SPCs. As seen before in Fig. 12(b), when a strong fiber like $F_{11}$ is composed with a brittle matrix like $M_{10}$, the SPC fails soon at $\check{e}^m = 0.09$ (scenario 2) which is far from the mean failure strain of this fiber where its maximum stress bearing capacity is. In this case, as plotted in Fig. 14(a), although the variation in $\check{\tau}$ does not affect the strength of the SPC, however, the main effect is observed in increasing the toughness by extending the pull-out with low interfacial bonding. In Fig. 14(c), where the matrix is tough, the situation is completely opposite since the failure strain of matrix $M_2$ is higher than that of $F_{11}$ (scenario 1) even for high interfacial bonding, $\check{\tau} = 5$. In this case, increasing $\check{\tau}$ significantly increases the strength of the SPC because the failure strain of the composite is the failure strain of the fiber bundle. Note that it also increases the toughness of the SPC as the area under the curve before the complete breakage of the fibers (and SPC), however, the pull-out toughness is reduced when the interfacial shear stress decreases. For the intermediate matrix, $M_4$, presented in Fig. 14(b), the situation is a mixture of cases (a) and (c) because the variation in $\check{\tau}$ switches the failure scenario as discussed before in Fig. 12(b). Unlike the fact that increasing the interfacial bonding *always* results in a higher strength of the SPC, a lower interfacial bonding that allows for considerable pull-out toughness may be an optimized solution when both toughness and strength of the SPC have the same priority. In other words, it is possible to sacrifice a little in strength to gain more in toughness.

To have a better insight into the SPC made of $F_{11}$, Fig. 15(a) and (b) plot the enhancement in its toughness and the strength normalized to the neat matrix $M_{10}$. One can see that when the matrix is brittle, i.e., $M_{10}$, although the strength of SPC is not affected by the interfacial shear, however, the toughness decreases due to a reduction in average pull-out length. Note that for very low interfacial shears, the toughness is a little raising and then it drops. The reason is that for such low values of $\check{\tau}$ the pull-out length reaches its assumed upper limit (see the first horizontal part of $F_{11}$ in Fig. 10) and therefore $\langle l_p \rangle$ is constant with respect to $\check{\tau}$. However, increasing $\check{\tau}$ slightly increases $\sigma^*$ which increases the pull-out work defined in Eq. (34). For the intermediate,

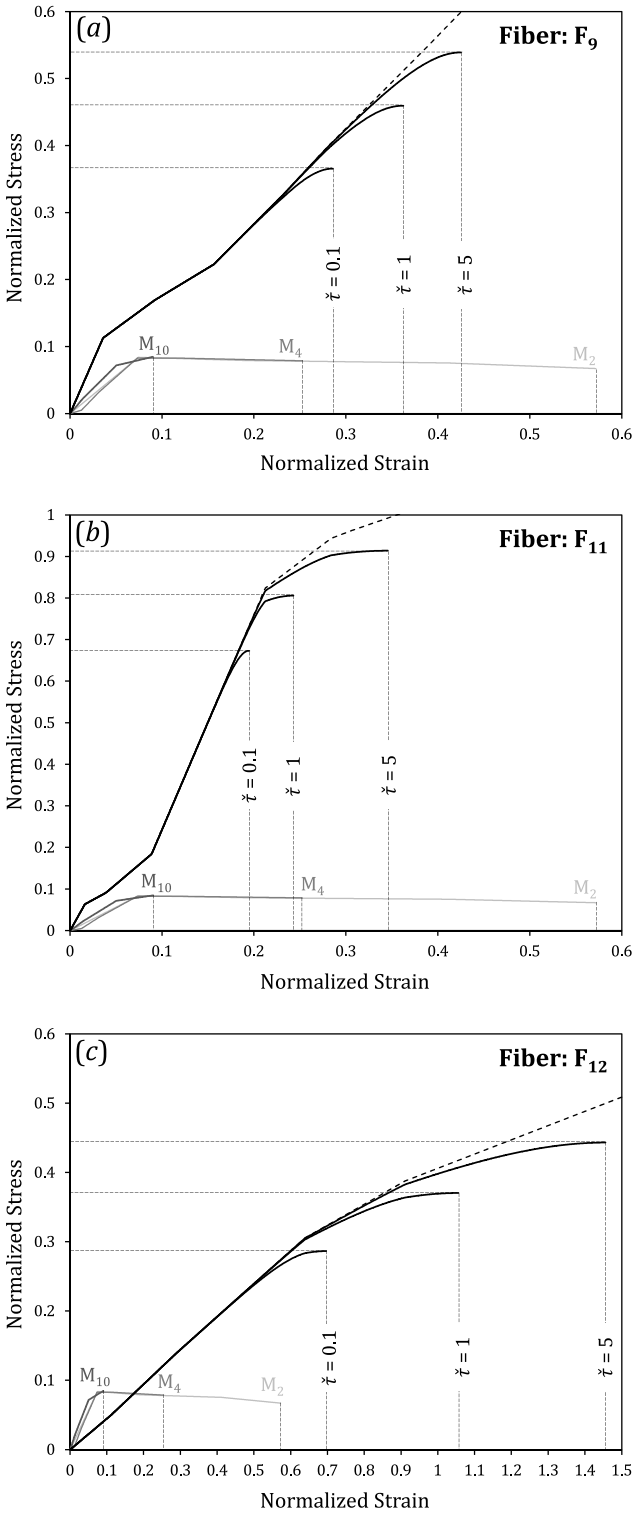


**Fig. 12.** Normalized stress–strain curve of the bundles of selected PA6 fibers for different normalized interfacial shear stress, $\check{\tau} = 0.1, 1,$ and 5 compared to the selected matrices. (a) $F_9$, (b) $F_{11}$, and (c) $F_{12}$.

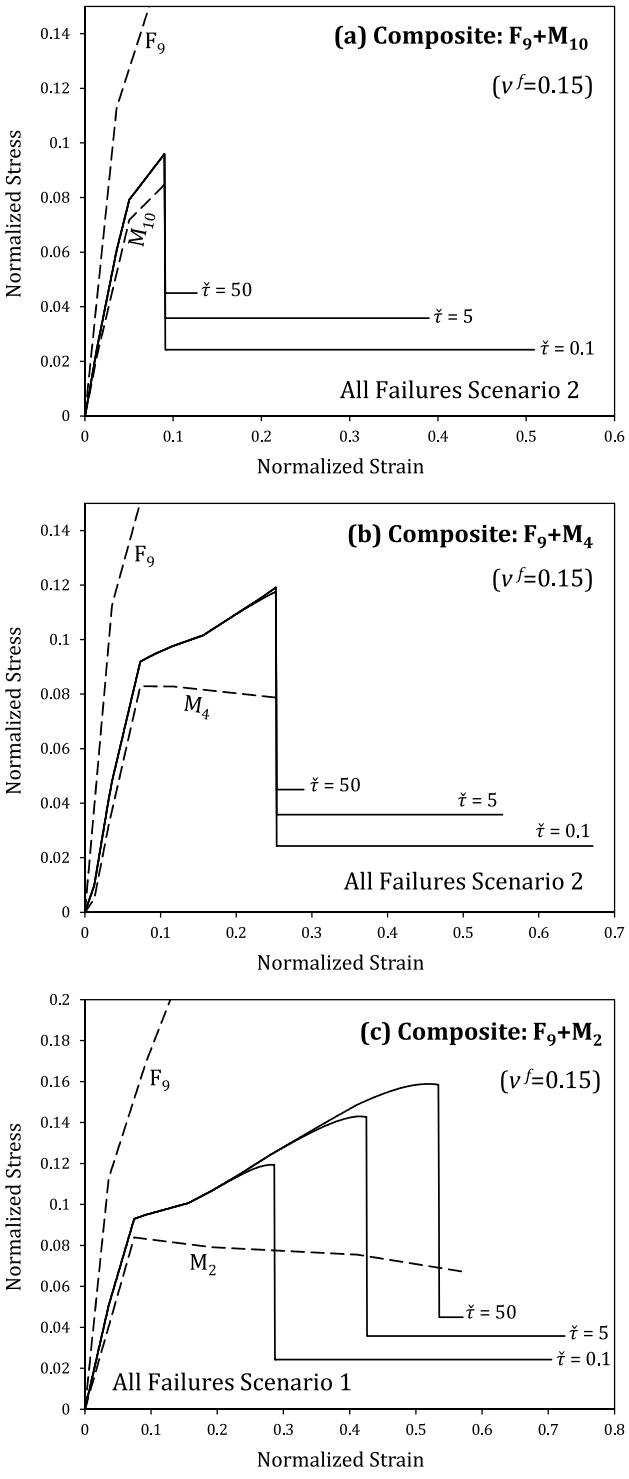


**Fig. 13.** Normalized stress–strain curves of the SPC composed of fiber $F_9$ with volume fraction $v^f = 0.15$ and for different normalized interfacial shear stress, $\check{\tau} = 0.1, 5,$ and 50. (a) The brittle matrix, $M_{10}$, (b) the intermediate matrix, $M_4$, and (c) the tough matrix, $M_2$.

$M_4$, and tough, $M_2$, matrices the strength increases by increasing the interfacial shear because by increasing $\check{\tau}$ the effective strength of the bundle increases and enough elongation of $M_4$ and $M_2$ before failure allow for taking the reinforcing effect of $F_{11}$. For the toughness, $M_4$ and $M_2$ have different stories with variation in $\check{\tau}$. When the matrix is tough with proper failure strain, increasing the interfacial shear stress allows the stress–strain curve of the SPC to rise up and consequently, the area under the curve adequately increases which is more important than losing the pull-out toughness. For the intermediate matrix, $M_4$, around $\check{\tau} = 1.3$ the failure strain of the fiber bundles reaches the failure strain of the matrix, and therefore the failure scenario switches from 1

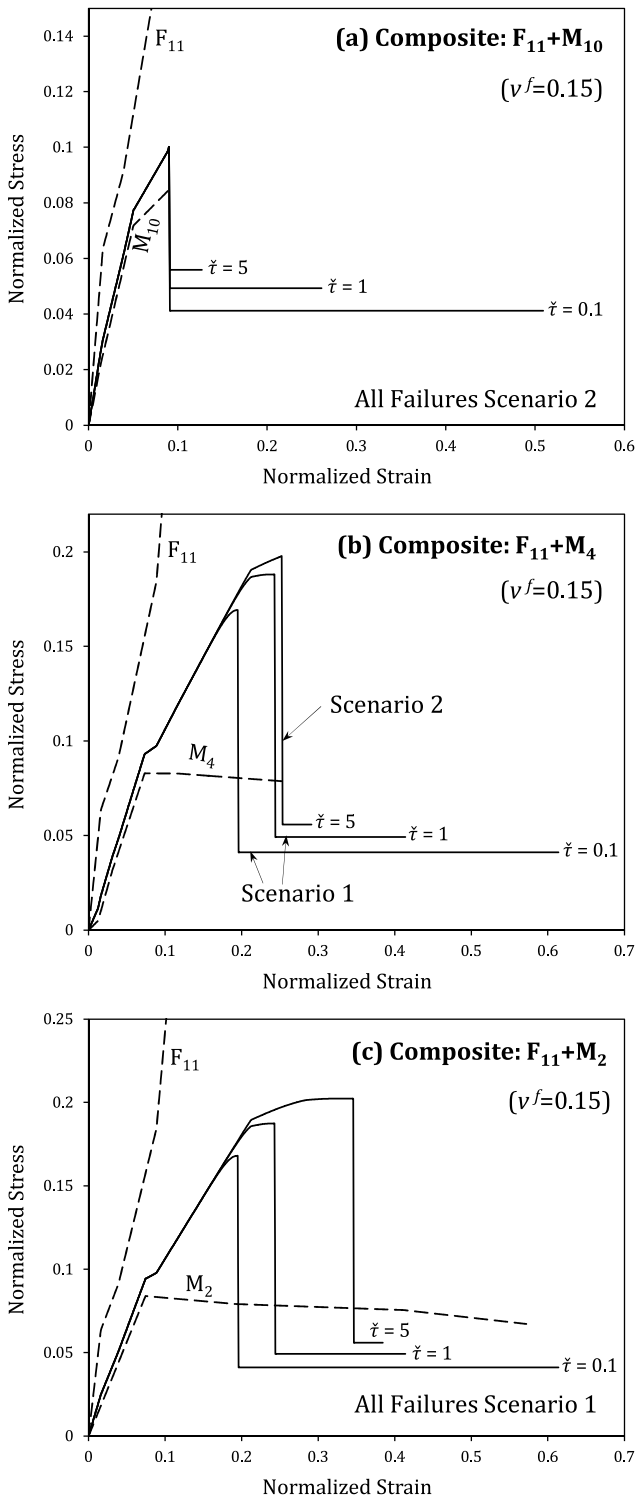


**Fig. 14.** Normalized stress–strain curves of the SPC composed of fiber $F_{11}$ with volume fraction $v^f = 0.15$ and for different normalized interfacial shear, $\check{\tau} = 0.1, 1,$ and 5. (a) The brittle matrix, $M_{10}$, (b) the intermediate matrix, $M_4$, and (c) the tough matrix, $M_2$.

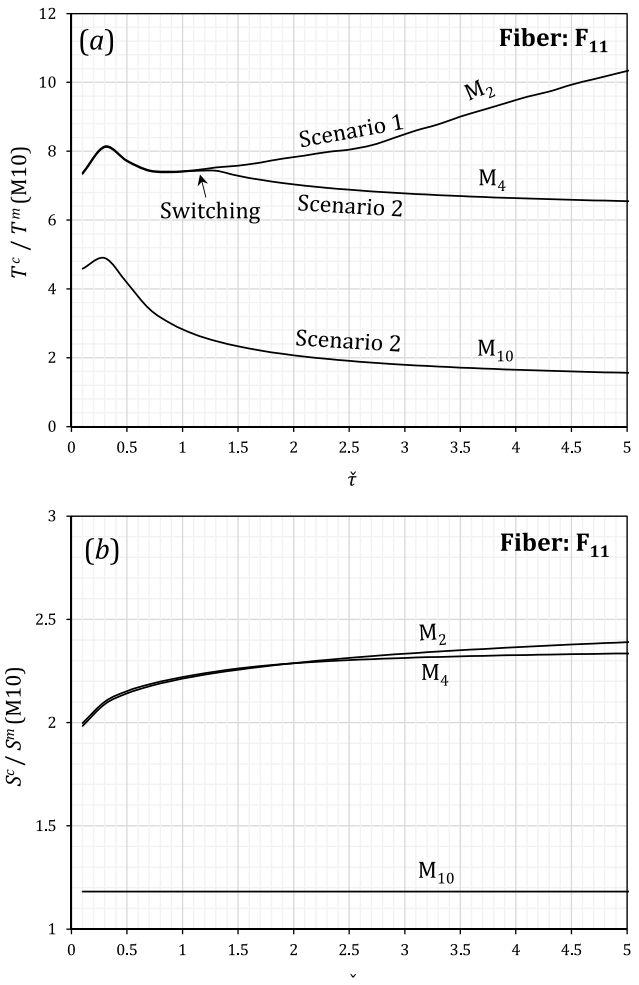


**Fig. 15.** Variation in the properties of the SPC composed of $F_{11}$ with volume fraction $v^f = 0.15$ as a function of normalized interfacial shear, $\check{\tau}$. (a) The toughness of composite with respect to the matrix $M_{10}$, (b) the strength of composite with respect to the matrix $M_{10}$.

to 2 which means the increase in $\check{\tau}$ does not enhance the stress–strain curve of the SPC and only causes a reduction in the pull-out toughness which means the total toughness of the SPC decreases.

Fig. 16 presents the normalized stress–strain curves for the SPC made of the most flexible fiber, $F_{12}$, with the volume fraction of $v^f = 0.15$. As described earlier in Fig. 12(c), the failure strain of this fiber remains always higher than that of the matrices even for tough $M_2$, and the failure of the SPC is always led by scenario 2. Note that the mean failure strain of $F_{12}$ is $\check{\varepsilon}_f = 1$, where its maximum loading capacity is located. Hence, it is difficult to take its strengthening effect since the failure strain of the matrix is around $\check{\varepsilon}^m = 0.57$ in the best case for the tough matrix, $M_2$. It is seen from Fig. 16(a) that for the brittle matrix, $M_{10}$, the strength of the SPC is even lower than that of the matrix, however, the pull-out phenomenon may be considered as a mechanism to enhance the toughness significantly. From Fig. 16(c) one can observe that when the matrix elongates more, the SPC can slightly experience the reinforcing effect of the fiber $F_{12}$. Besides, it is seen that for $\check{\varepsilon}^m$ around 0.57 (matrix $M_2$) the pull-out almost vanishes which means a strong almost fully bonded interface between $F_{12}$ and the matrix has formed due to its non-circular thin cross-section and relatively low strength compared to $S_9$ and $S_{11}$.

Until here a detailed investigation of the influence of interfacial shear stress on the properties of the PA6 SPCs made of the combination of three selected fibers is presented: the thickest, $F_9$, the strongest, $F_{11}$, and the most ductile, $F_{12}$ and three representative matrices: brittle, $M_{10}$, intermediate, $M_4$, and tough, $M_2$. As the final prediction, the whole available design area of PA6-based SPCs according to the experimental measurements in Section 3 is demonstrated. Combination of 12 fibers, $F_1$, to $F_{12}$, with 10 matrices, $M_1$ to $M_{10}$, considering five values for the normalized interfacial shear, $\check{\tau} = 0.25$, 0.5, 1, 3, and 5, results in

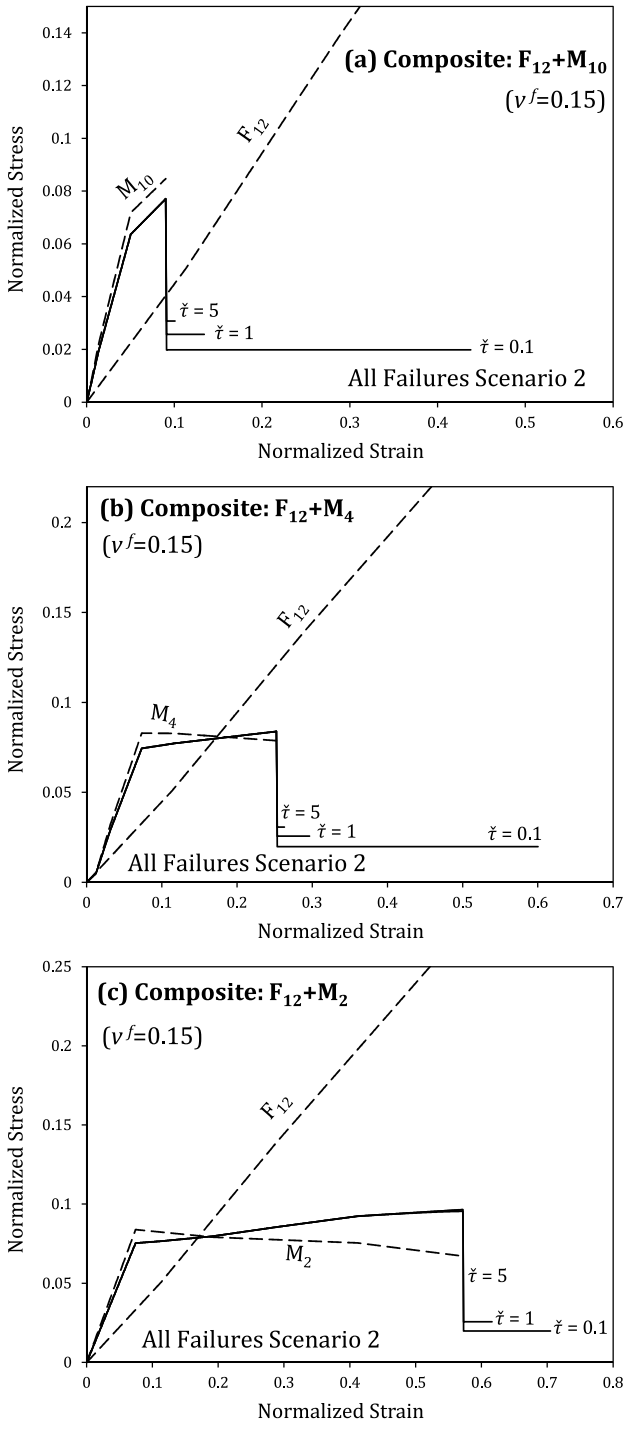


**Fig. 16.** Normalized stress–strain curves of the SPC composed of fiber $F_{12}$ with volume fraction $v^f = 0.15$ and for different normalized interfacial shear, $\check{\tau} = 0.1, 1,$ and 5. (a) The brittle matrix, $M_{10}$, (b) the intermediate matrix, $M_4$, and (c) the tough matrix, $M_2$.

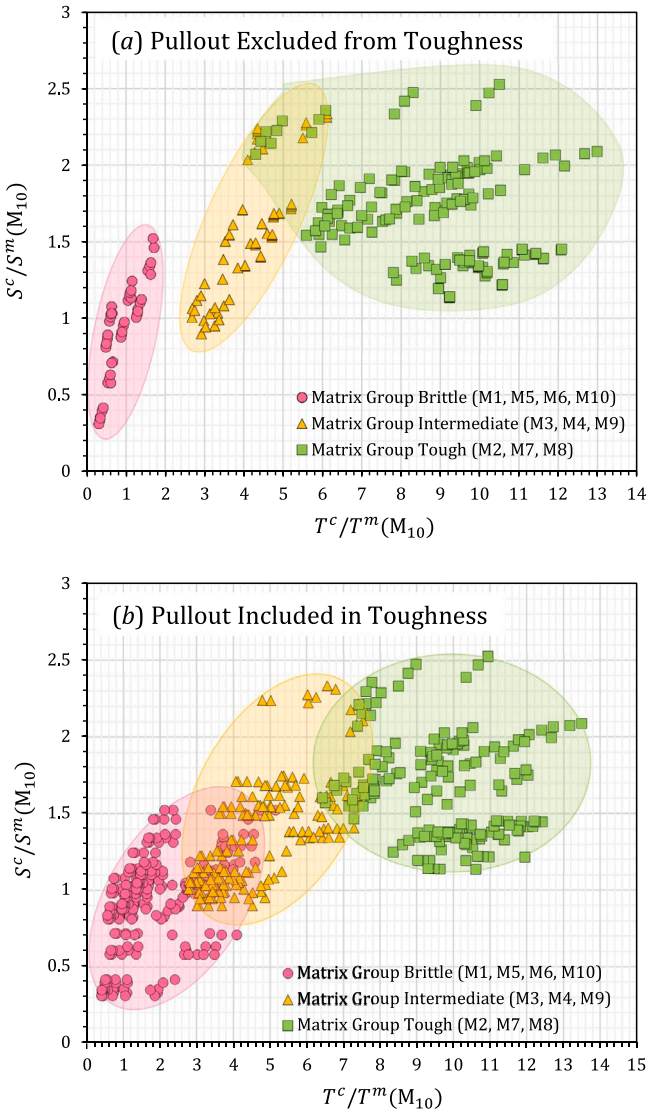


**Fig. 17.** Ashby plot (strength versus toughness) for all 600 possible combinations of PA6 SPCs, i.e., 12 fibers and 10 matrices listed in Table 1 and for five different normalized interfacial shearing strengths, $\check{\tau} = 0.25$, 0.5, 1, 3, and 5. (a) Neglecting pull-out toughness, $T_p$, introduced in Eq. (36), (b) taking into account the extra toughness of pull-out.

600 different PA6-based SPCs whose predicted properties are plotted in a strength-versus-toughness Ashby plot in Fig. 17. Note that while the model does not explicitly consider the impact of process parameters like temperature and time on composite properties, the influence of these parameters is introduced into the model by explicitly incorporating a range of interfacial shear strength values from weak to strong for each fiber–matrix combination. The strength and the toughness of the SPCs are normalized with respect to the representative brittle matrix, $M_{10}$, to reveal the enhancement in the properties of the SPCs. Fig. 17(a) neglects the extra toughness due to the pull-out defined in Eq. (36) while Fig. 17(b) includes it. The results are separated into three groups according to the categories of the matrices defined before, i.e., brittle, intermediate, and tough because the failure strain of the matrix plays a vital role in the failure scenario of the SPCs. In general, it is seen that the maximum enhancement in both the strength and the toughness belongs to the tough matrices group and the minimum is for the brittle group. The Ashby plot shows that SPC reinforced with a PA6 fiber and tough matrix can achieve a toughness over 13 times, or strength over 2.5 times of a neat brittle PA6 like $M_{10}$ which means a huge design area for optimization of the PA6-based SPCs exist.

Besides, in general, the pull-out mechanism results in an enhancement in the toughness of the SPCs which is more noticeable in the brittle and intermediate groups. This observation is demonstrated in more detail in Fig. 18 which plots the Ashby plot for brittle and tough

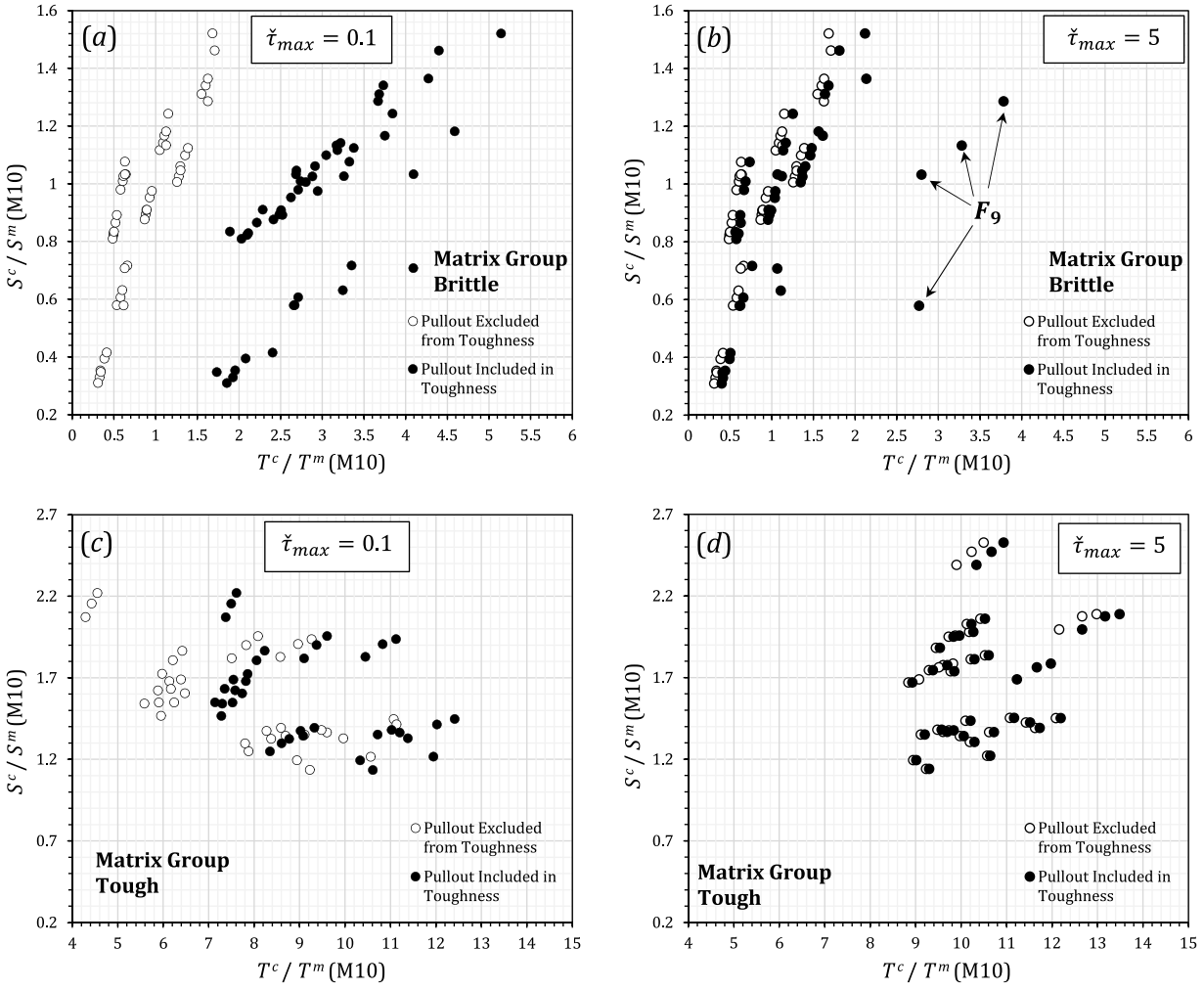


**Fig. 18.** More detailed illustrations of the effect of pull-out on the Ashby plots (strength versus toughness) of PA6 SPCs. (a) Brittle matrices with $\check{\tau} = 0.1$ (b) brittle matrices with $\check{\tau} = 5$, (c) tough matrices with $\check{\tau} = 0.1$, and (d) tough matrices with $\check{\tau} = 5$.

groups and for two normalized interfacial shear stresses, $\check{\tau} = 0.1$ and 5. Hollow points neglect the pull-out and the solid ones include the extra toughness from the pull-out. One can conclude that the pull-out affects the toughness more when the matrix is brittle. In addition, it is shown that the pull-out has a significant role when the interfacial shear stress is low. The reason is that the lower the interfacial shear, the higher the average pull-out length. In Fig. 17(b) one can notice that for $\check{\tau} = 5$ the pull-out significantly enhances the toughness of SPC made of $S_9$. It is not surprising since it is revealed before in Fig. 10 that $S_9$ presents a high pull-out length at $\check{\tau} = 5$. It is due to the fact that $\check{\tau} = 5$ is equivalent to 500% and 2500% of the characteristic interfacial shear stress, $\tau^*$, of fibers $F_{11}$ and $F_{12}$, respectively, while it is only 59% of $\tau^*_{(F_9)}$. In other words, $\check{\tau} = 5$ does not present a high enough interfacial bonding for $F_9$ as a result of its circular thick cross-section.

## 5. Conclusion

A novel analytical progressive micromechanics model is developed to predict the stress–strain curve of composites reinforced by continuous or discontinuous aligned fibers based on the well-known Curtin statistical progressive fiber breakage model. The proposed model considers the nonlinear behavior of the components which makes it ideal for better SPCs and the classical shear lag assumption is modified to take into account the concentration of interfacial shearing stress at the tip of broken fibers, and a non-circular cross-section of fibers which is common in polymeric fibers. The model also captures the extra after-breakage toughness due to the pull-out of the fibers.

In order to test the ability of the model, PA6-based SPCs are selected and extensive sets of experimental measurements on the properties of both PA6 fibers and PA6 matrices are carried out to determine the achievable space design of PA6-based SPCs. Tensile tests on 12 different available PA6 fibers are performed (at least 5 repetitions per fiber type) and after an initial assessment of the stress–strain curves, three fibers, i.e., the thickest ($F_9$), the strongest ($F_{11}$), and the most ductile ($F_{12}$), are selected and extra repetitions of the tensile tests are performed to achieve reliable Weibull statistical parameters for more investigations. In addition, 10 PA6 matrices are polymerized using different types of PA6 raw materials and various dosages of additives and tested by a tensile test machine providing a wide range of failure strains from brittle to tough (about 5% to over 60%).

Being employed as the inputs of the progressive model, the experimentally measured properties of the PA6 fibers and the PA6 matrices draw the whole achievable space for designing the PA6-based SPCs. The two main properties extracted from the predicted stress–strain curves of these SPCs are strength and toughness (as the area under the curve)

which are plotted in the form of Ashby plots for a better demonstration of conclusions. It reveals that there is considerable potential for enhancement in both the strength and toughness of neat PA6 matrix reinforced by PA6 fibers forming recyclable PA6-based SPCs. Besides, the vital role of interfacial shear stress on the properties of the SPCs is demonstrated in the results. The output of the progressive model shows that the modification of interfacial shear stress may switch the failure scenario. The reason is that the failure strain of the fiber bundle is significantly shifted by varying the interfacial shear stress and therefore the failure strain of a specific fiber may be lower or higher than that of the matrix depending on the strength of interfacial bonding. This phenomenon may not be noticeable in fiber-reinforced composites with brittle fibers like glass or carbon where the failure strain of fibers is normally lower than that of the matrix. However, in the case of SPCs where flexible polymeric fibers provide high failure strains, the fact that the failure strain can be tailored by the interfacial shear stress is a key parameter for optimal design, especially where both strength and toughness are important. Note that the extra pull-out toughness is strongly dependent on the interfacial shear stress.

Given the presented Ashby plot, it is revealed that the composite manufacturing path must aim to converge towards the absolute optimal point where both the strength and toughness are maximum. However, practical considerations in the manufacturing process and a cost-benefit margin tailored to a specific product might lead to the selection of alternative points on the Ashby plot. For instance, achieving the highest performance necessitates making the highest possible shear strength at the fiber–matrix interface, a task that may prove challenging or expensive in practical manufacturing processes, potentially increasing the overall cost of mass production. Additionally, in certain applications like impact loading, toughness may be prioritized over strength, introducing a scenario where the significance of these properties is not identical. In such cases, a fiber–matrix combination that meets requirements at a lower cost, perhaps due to the selection of more economical fibers or a simpler manufacturing process, could be a more optimized choice compared to the absolute optimal combination offering the highest strength and toughness simultaneously. In conclusion, the present word proves that the proposed progressive micromechanical model in conjunction with the given experimental inputs constructs a parametric analytical framework for designing new recyclable SPCs with desired mechanical performance.

## CRediT authorship contribution statement

**S.K. Jalali:** Conceptualization, Formal analysis, Methodology, Software, Validation, Visualization, Writing – original draft, Writing – review & editing, Data curation, Investigation. **G. Greco:** Data curation, Investigation, Validation, Writing – review & editing. **D. Rigotti:** Data curation, Investigation, Validation. **A. Dorigato:** Supervision. **H. Mirbaha:** Data curation, Investigation. **G. Fredi:** Conceptualization, Data curation, Investigation, Validation, Visualization, Writing – review & editing. **M. Bertolla:** Conceptualization, Project administration, Resources, Writing – review & editing. **S. Guerra:** Resources. **T. Battistini:** Conceptualization, Project administration, Resources, Supervision. **A. Dal Moro:** Conceptualization, Funding acquisition, Project administration, Resources, Supervision. **A. Pegoretti:** Conceptualization, Funding acquisition, Methodology, Project administration, Supervision, Writing – review & editing. **N.M. Pugno:** Conceptualization, Formal analysis, Funding acquisition, Methodology, Project administration, Supervision, Writing – review & editing.

## Data availability

No data was used for the research described in the article.

## Acknowledgments

This work was produced with the co-funding of the European Union - FSE-REACT-EU, PON Research and Innovation 2014–2020 DM1062/2021.

## Appendix. Stess-strain curve fittings

In this appendix the step-by-step procedure of the approach used for converting the original stress–strain curve to an approximated $N$-segmented one compatible with Eq. (1) is explained.

*Step 1*: As there is more than one stress–strain curve per material (each fiber or each matrix), the one with the failure strain closest to the mean failure strain is selected as the representative stress–strain curve and it is normalized to its maximum stress (strength) and its maximum strain (failure strain). Hence, the normalized curve always starts at the origin (0, 0) and ends at (1, 1) if the maximum stress happens at failure strain (compare $F_1$ in Fig. A.2 and $M_2$ in Fig. A.6).

*Step 2*: The normalized representative stress–strain curve is interpolated by a 6th-order polynomial, $\tilde{\sigma} = f(\tilde{\varepsilon})$, and the inflection points are found as the roots of $\frac{d^2(f)}{d(\tilde{\varepsilon})} = 0$. The maximum number of roots is four dividing the stress–strain curve into five pieces of arcs. Note that regarding the shape of the curve, the number of pieces may be less.

*Step 3*: An intermediate point is picked up on each piece enclosed between two inflection points by the procedure graphically demonstrated in Fig. A.1(a).

*Step 4*: The approximated segmented stress–strain curve is constructed by connecting the inflection and intermediate points one after another.

*Step 5*: Two adjacent segments are unified when the difference in the slope is less than 5% by removing the common point, see Fig. A.1(b).

*Step 6*: The 6th-order polynomial cannot follow the almost straight portion of stress–strain curves that may be observed where the matrix is yielded or the behavior of fibers is linear. In these cases, the pseudo-inflection points are removed to avoid unrealistic fluctuation in the segmented curve, see $M_4$ in Fig. A.7.

*Step 7*: The 6th-order polynomial also cannot follow the very local peaks in stress–strain curves that may be observed around the yielding point of the matrix. In these cases, a manual shift is applied to the point closest to the peak to improve the accuracy of the segmented curve compared to the original one.

Figs. A.2 to A.9 graphically present the approximated $N$-segmented stress–strain curves for the fibers $F_1$ to $F_{12}$, and the matrices $M_1$ to $M_{10}$. In addition, the coordinates of the points and the slopes of the linear segments are listed for the PA6 fibers and the matrices in Table A.1 and Table A.2, respectively.

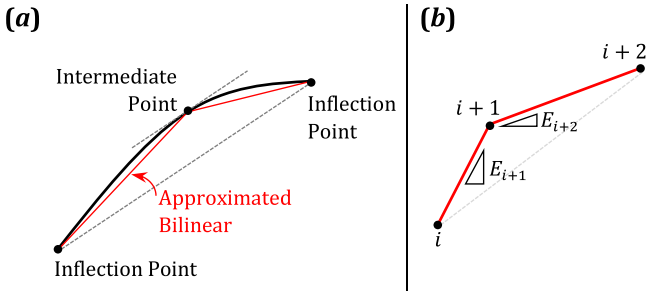


**Fig. A.1.** The schematic of approximating the stress–strain curve with an $N$-segmented curve.

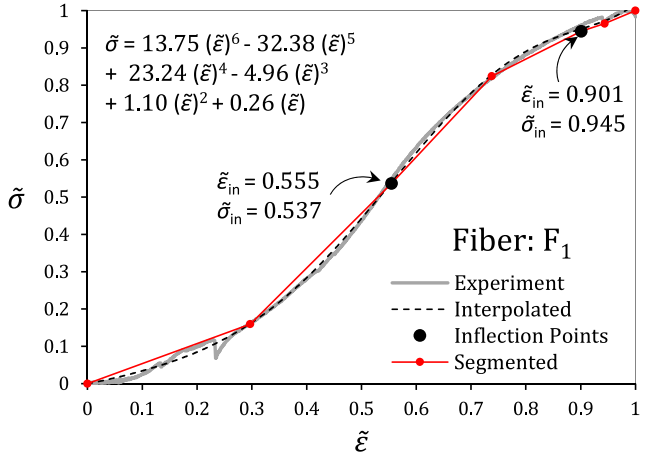


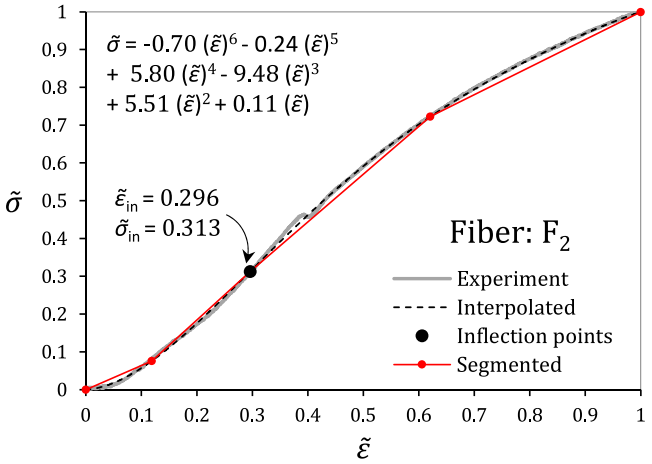


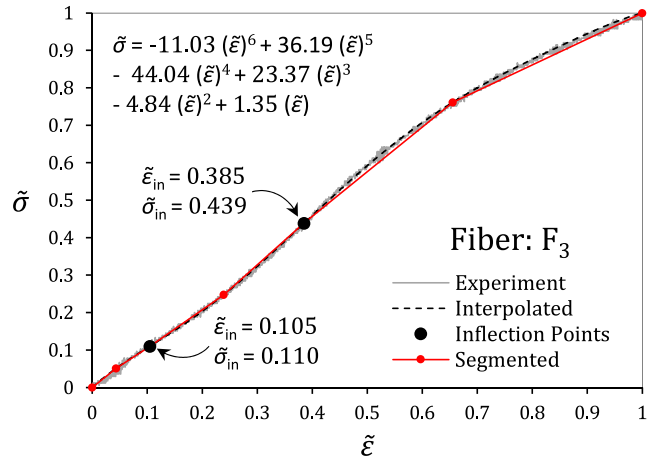


**Fig. A.2.** The normalized approximated stress–strain curves of PA6 fibers ($F_1$ to $F_3$).

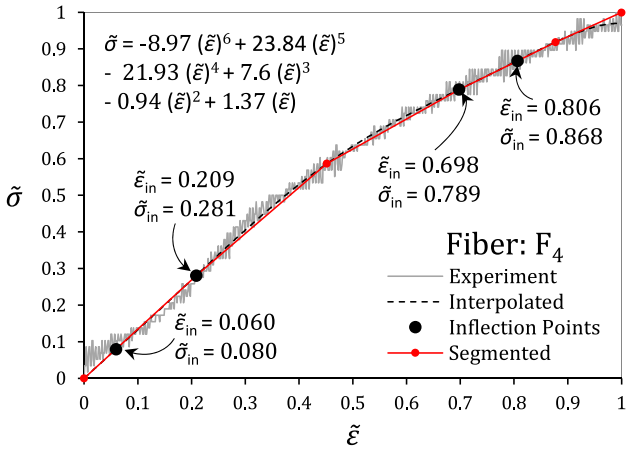


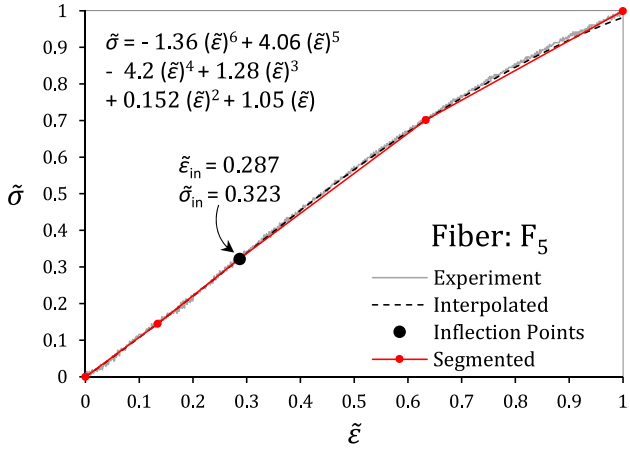


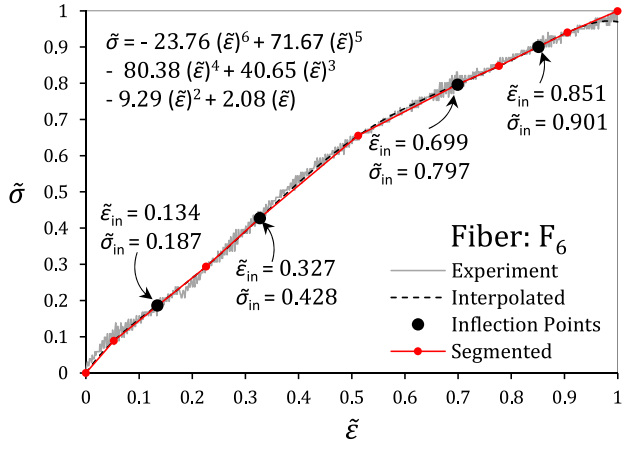


**Fig. A.3.** The normalized approximated stress–strain curves of PA6 fibers ($F_4$ to $F_6$).

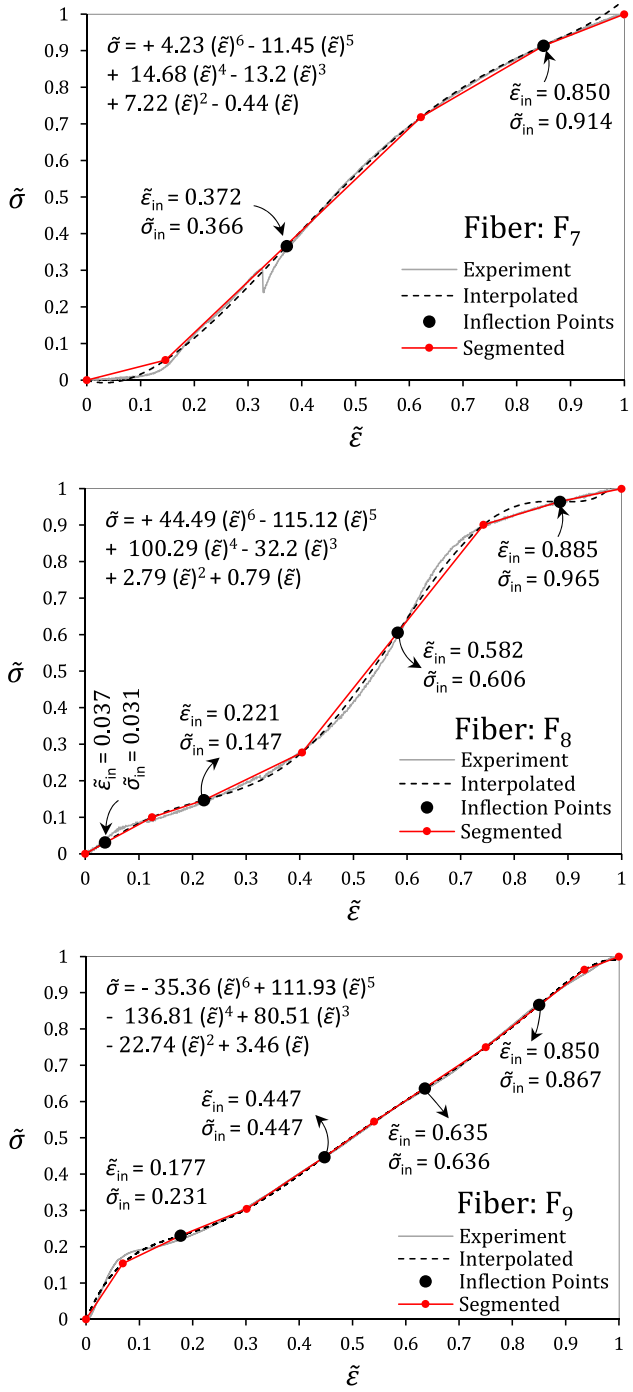


**Fig. A.4.** The normalized approximated stress–strain curves of PA6 fibers ($F_7$ to $F_9$).

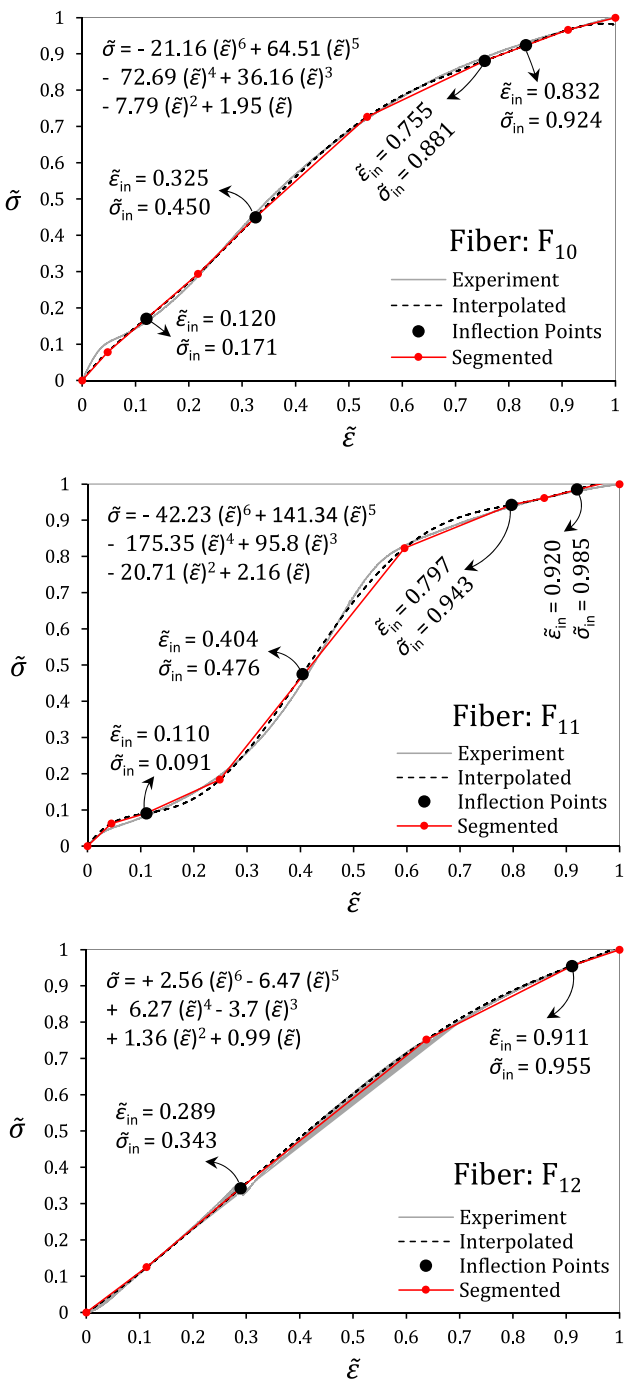


**Fig. A.5.** The normalized approximated stress–strain curves of PA6 fibers ($F_{10}$ to $F_{12}$).

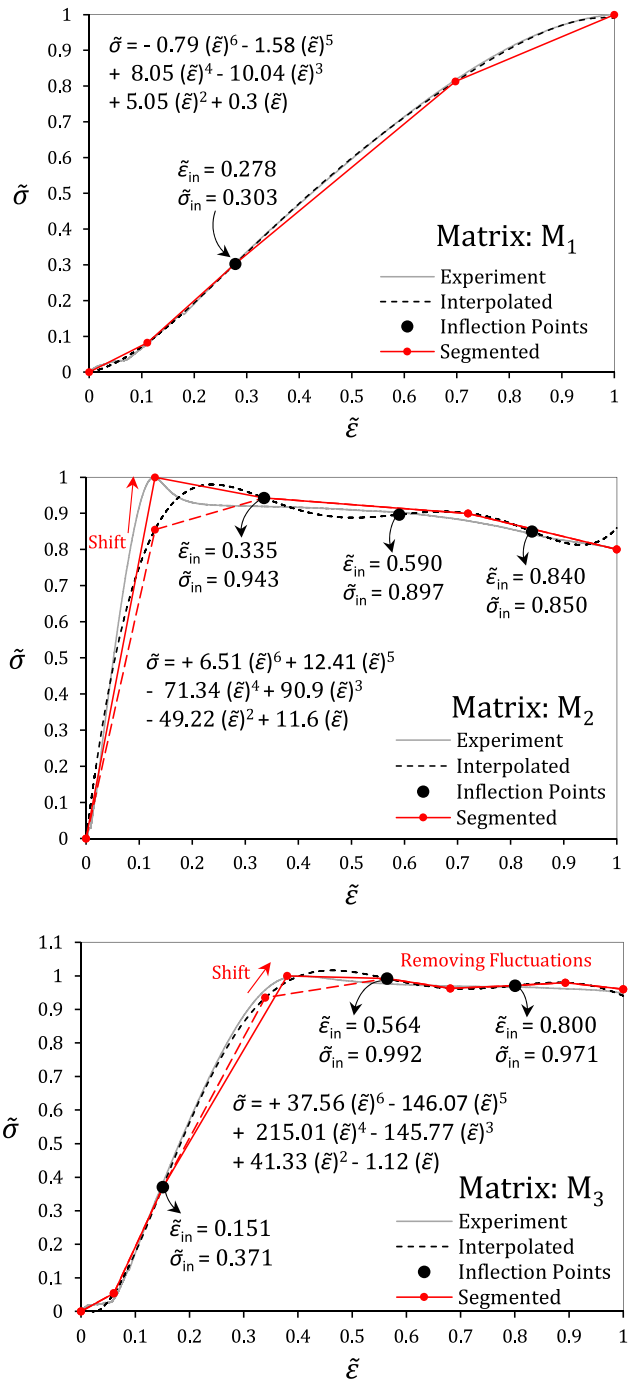


**Fig. A.6.** The normalized approximated stress–strain curves of PA6 matrices ($M_1$ to $M_3$).

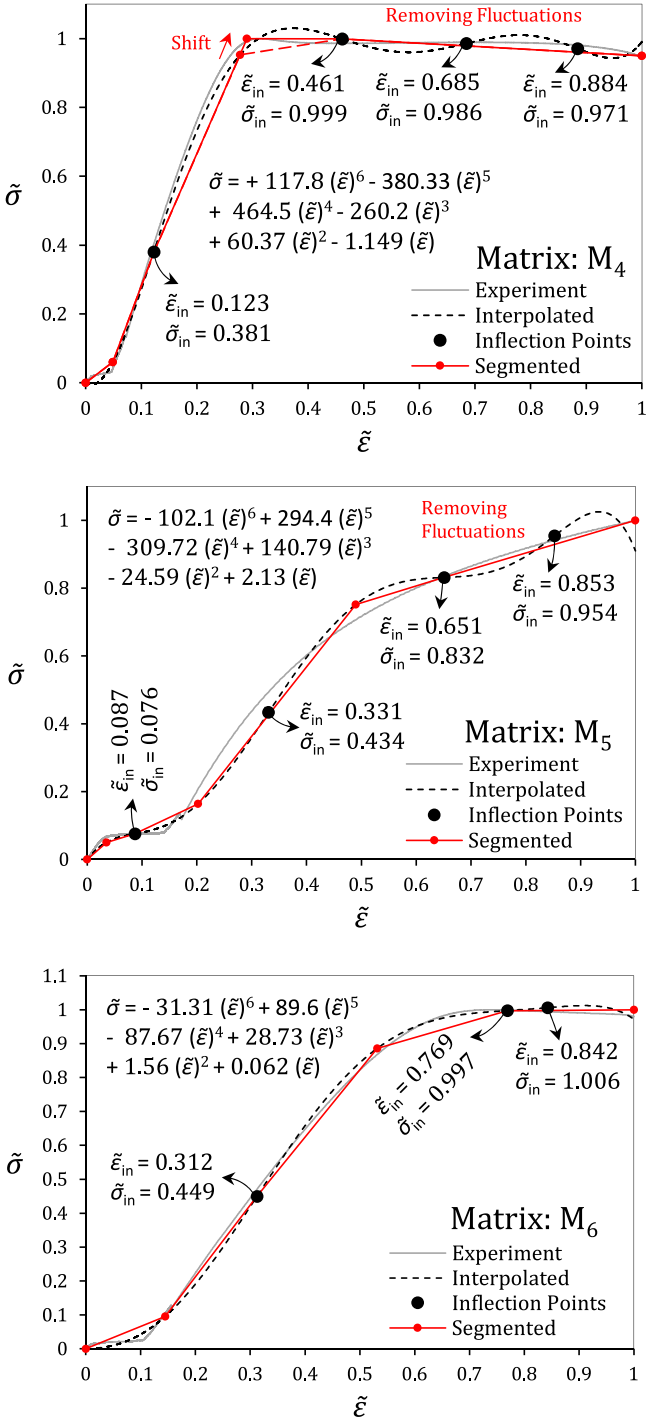


**Fig. A.7.** The normalized approximated stress–strain curves of PA6 matrices ($M_4$ to $M_6$).

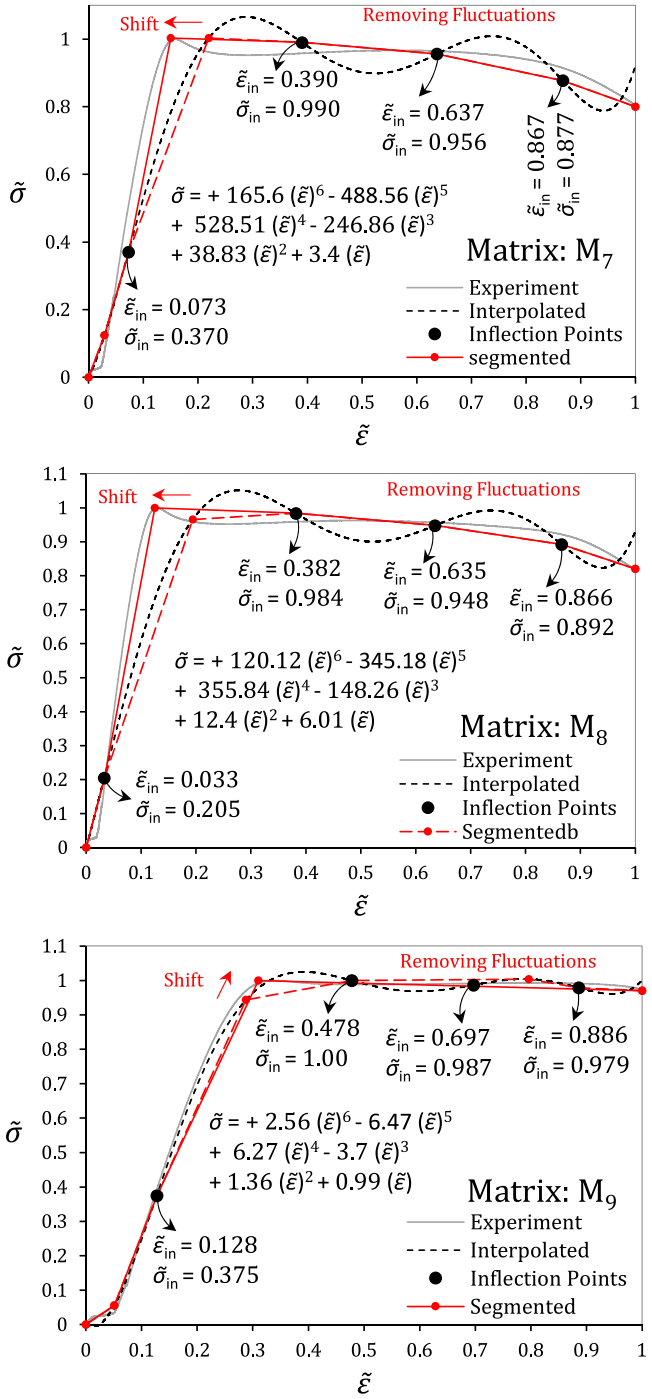


**Fig. A.8.** The normalized approximated stress–strain curves of PA6 matrices ($M_7$ to $M_9$).

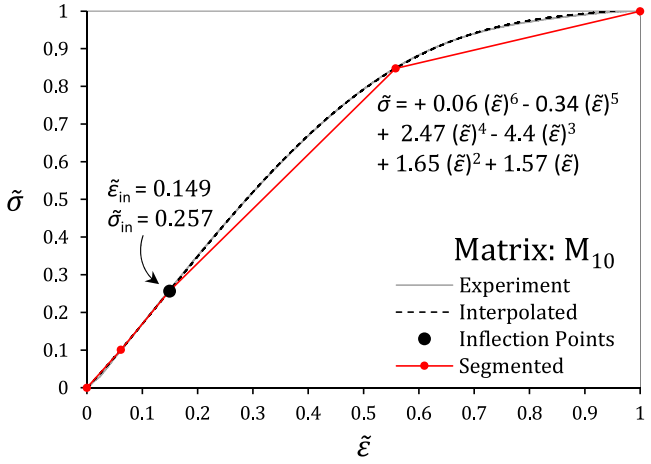


**Fig. A.9.** The normalized approximated stress–strain curves of PA6 matrix $M_{10}$.

**Table A.1**
The $N$-segmented approximation of the dimensionless stress–strain curves of the PA6 fibers.

| Fiber | | Segments, $i$ | | | | | | | |
|---|---|---|---|---|---|---|---|---|---|
| | | 0 | 1 | 2 | 3 | 4 | 5 | 6 | 7 |
| $F_1$ | $\tilde{\varepsilon}_i$ | 0 | 0.297 | 0.555 | 0.738 | 0.901 | 1 | | |
| | $\tilde{\sigma}_i$ | 0 | 0.160 | 0.537 | 0.824 | 0.945 | 1 | | |
| | $\tilde{E}_i$ | – | 0.538 | 1.463 | 1.569 | 0.742 | 0.556 | | |
| $F_2$ | $\tilde{\varepsilon}_i$ | 0 | 0.119 | 0.296 | 0.621 | 1 | | | |
| | $\tilde{\sigma}_i$ | 0 | 0.076 | 0.313 | 0.723 | 1 | | | |
| | $\tilde{E}_i$ | – | 0.641 | 1.337 | 1.262 | 0.730 | | | |
| $F_3$ | $\tilde{\varepsilon}_i$ | 0 | 0.044 | 0.105 | 0.239 | 0.385 | 0.655 | 1 | |
| | $\tilde{\sigma}_i$ | 0 | 0.051 | 0.110 | 0.248 | 0.439 | 0.761 | 1 | |
| | $\tilde{E}_i$ | – | 1.179 | 0.954 | 1.028 | 1.310 | 1.192 | 0.693 | |
| $F_4$ | $\tilde{\varepsilon}_i$ | 0 | 0.209 | 0.452 | 0.698 | 0.877 | 1 | | |
| | $\tilde{\sigma}_i$ | 0 | 0.281 | 0.587 | 0.789 | 0.919 | 1 | | |
| | $\tilde{E}_i$ | – | 1.344 | 1.259 | 0.822 | 0.726 | 0.659 | | |
| $F_5$ | $\tilde{\varepsilon}_i$ | 0 | 0.134 | 0.287 | 0.633 | 1 | | | |
| | $\tilde{\sigma}_i$ | 0 | 0.145 | 0.323 | 0.701 | 1 | | | |
| | $\tilde{E}_i$ | – | 1.084 | 1.161 | 1.092 | 0.815 | | | |
| $F_6$ | $\tilde{\varepsilon}_i$ | 0 | 0.053 | 0.226 | 0.327 | 0.512 | 0.699 | 0.777 | 1 |
| | $\tilde{\sigma}_i$ | 0 | 0.089 | 0.294 | 0.428 | 0.656 | 0.797 | 0.848 | 1 |
| | $\tilde{E}_i$ | – | 1.693 | 1.183 | 1.324 | 1.230 | 0.756 | 0.651 | 0.683 |
| $F_7$ | $\tilde{\varepsilon}_i$ | 0 | 0.146 | 0.622 | 0.850 | 1 | | | |
| | $\tilde{\sigma}_i$ | 0 | 0.055 | 0.719 | 0.914 | 1 | | | |
| | $\tilde{E}_i$ | – | 0.374 | 1.397 | 0.854 | 0.573 | | | |
| $F_8$ | $\tilde{\varepsilon}_i$ | 0 | 0.037 | 0.125 | 0.221 | 0.404 | 0.742 | 0.885 | 1 |
| | $\tilde{\sigma}_i$ | 0 | 0.031 | 0.100 | 0.147 | 0.278 | 0.901 | 0.965 | 1 |
| | $\tilde{E}_i$ | – | 0.838 | 0.791 | 0.484 | 0.714 | 1.843 | 0.450 | 0.304 |
| $F_9$ | $\tilde{\varepsilon}_i$ | 0 | 0.069 | 0.177 | 0.301 | 0.447 | 0.541 | 0.750 | 1 |
| | $\tilde{\sigma}_i$ | 0 | 0.154 | 0.231 | 0.304 | 0.447 | 0.545 | 0.750 | 1 |
| | $\tilde{E}_i$ | – | 2.232 | 0.713 | 0.589 | 0.979 | 1.048 | 0.977 | 1.002 |
| $F_{10}$ | $\tilde{\varepsilon}_i$ | 0 | 0.048 | 0.217 | 0.325 | 0.535 | 0.755 | 0.912 | 1 |
| | $\tilde{\sigma}_i$ | 0 | 0.079 | 0.294 | 0.450 | 0.726 | 0.881 | 0.967 | 1 |
| | $\tilde{E}_i$ | – | 1.655 | 1.268 | 1.449 | 1.319 | 0.701 | 0.546 | 0.379 |
| $F_{11}$ | $\tilde{\varepsilon}_i$ | 0 | 0.045 | 0.110 | 0.249 | 0.596 | 0.797 | 0.858 | 1 |
| | $\tilde{\sigma}_i$ | 0 | 0.063 | 0.091 | 0.184 | 0.823 | 0.943 | 0.962 | 1 |
| | $\tilde{E}_i$ | – | 1.413 | 0.429 | 0.668 | 1.843 | 0.596 | 0.301 | 0.272 |
| $F_{12}$ | $\tilde{\varepsilon}_i$ | 0 | 0.113 | 0.289 | 0.638 | 0.911 | 1 | | |
| | $\tilde{\sigma}_i$ | 0 | 0.125 | 0.343 | 0.752 | 0.955 | 1 | | |
| | $\tilde{E}_i$ | – | 1.104 | 1.240 | 1.172 | 0.744 | 0.506 | | |

**Table A.2**
The $N$-segmented approximation of the dimensionless stress–strain curves of the PA6 matrices.

| Matrix | | Segments, $i$ | | | | | | | |
|---|---|---|---|---|---|---|---|---|---|
| | | 0 | 1 | 2 | 3 | 4 | 5 | 6 | 7 |
| $M_1$ | $\tilde{\varepsilon}_i$ | 0 | 0.110 | 0.278 | 0.698 | 1 | | | |
| | $\tilde{\sigma}_i$ | 0 | 0.082 | 0.303 | 0.813 | 1 | | | |
| | $\tilde{E}_i$ | – | 0.745 | 1.317 | 1.215 | 0.619 | | | |
| $M_2$ | $\tilde{\varepsilon}_i$ | 0 | 0.130 | 0.335 | 0.720 | 1 | | | |
| | $\tilde{\sigma}_i$ | 0 | 1 | 0.943 | 0.900 | 0.800 | | | |
| | $\tilde{E}_i$ | – | 7.710 | −0.278 | −0.113 | −0.355 | | | |
| $M_3$ | $\tilde{\varepsilon}_i$ | 0 | 0.060 | 0.151 | 0.380 | 0.564 | 1 | | |
| | $\tilde{\sigma}_i$ | 0 | 0.054 | 0.371 | 1 | 0.992 | 0.960 | | |
| | $\tilde{E}_i$ | – | 0.891 | 3.501 | 2.747 | −0.043 | −0.073 | | |
| $M_4$ | $\tilde{\varepsilon}_i$ | 0 | 0.049 | 0.123 | 0.29 | 0.461 | 1 | | |
| | $\tilde{\sigma}_i$ | 0 | 0.060 | 0.381 | 1 | 0.999 | 0.950 | | |
| | $\tilde{E}_i$ | – | 1.233 | 4.328 | 3.707 | −0.006 | −0.091 | | |
| $M_5$ | $\tilde{\varepsilon}_i$ | 0 | 0.035 | 0.087 | 0.202 | 0.490 | 0.651 | 1 | |
| | $\tilde{\sigma}_i$ | 0 | 0.050 | 0.076 | 0.164 | 0.752 | 0.832 | 1 | |
| | $\tilde{E}_i$ | – | 1.427 | 0.499 | 0.765 | 2.042 | 0.499 | 0.481 | |
| $M_6$ | $\tilde{\varepsilon}_i$ | 0 | 0.145 | 0.312 | 0.532 | 0.769 | 1 | | |
| | $\tilde{\sigma}_i$ | 0 | 0.096 | 0.449 | 0.886 | 0.997 | 1 | | |
| | $\tilde{E}_i$ | – | 0.660 | 2.112 | 1.989 | 0.469 | 0.013 | | |
| $M_7$ | $\tilde{\varepsilon}_i$ | 0 | 0.029 | 0.073 | 0.150 | 0.390 | 0.637 | 0.867 | 1 |
| | $\tilde{\sigma}_i$ | 0 | 0.124 | 0.370 | 1 | 0.990 | 0.956 | 0.877 | 0.800 |
| | $\tilde{E}_i$ | – | 4.324 | 5.551 | 8.182 | −0.042 | −0.138 | −0.343 | −0.579 |
| $M_8$ | $\tilde{\varepsilon}_i$ | 0 | 0.033 | 0.125 | 0.382 | 0.635 | 0.866 | 1 | |
| | $\tilde{\sigma}_i$ | 0 | 0.205 | 1 | 0.984 | 0.948 | 0.892 | 0.820 | |
| | $\tilde{E}_i$ | – | 6.212 | 8.641 | −0.062 | −0.142 | −0.242 | −0.537 | |
| $M_9$ | $\tilde{\varepsilon}_i$ | 0 | 0.051 | 0.128 | 0.310 | 1 | | | |
| | $\tilde{\sigma}_i$ | 0 | 0.056 | 0.375 | 1 | 0.970 | | | |
| | $\tilde{E}_i$ | – | 1.094 | 4.141 | 3.434 | −0.043 | | | |
| $M_{10}$ | $\tilde{\varepsilon}_i$ | 0 | 0.061 | 0.149 | 0.558 | 1 | | | |
| | $\tilde{\sigma}_i$ | 0 | 0.101 | 0.257 | 0.848 | 1 | | | |
| | $\tilde{E}_i$ | – | 1.655 | 1.773 | 1.446 | 0.344 | | | |

## References


[1] Capiati Numa J, Porter Roger S. The concept of one polymer composites modelled with high density polyethylene. J Mater Sci 1975;10(10):1671–7. http://dx.doi.org/10.1007/BF00554928.

[2] Pegoretti Alessandro, Zanolli Andrea, Migliaresi Claudio. Preparation and tensile mechanical properties of unidirectional liquid crystalline single-polymer composites. Compos Sci Technol 2006;66(13):1970–9. http://dx.doi.org/10.1016/j.compscitech.2006.01.012.

[3] Kharbanda Sugeet, Bhadury Tanish, Gupta Gaurav, Fuloria Devasri, Pati Pravat Ranjan, Mishra Vijay Kumar, et al. Polymer composites for thermal applications - a review. Mater Today Proc 2021;47:2839–45. http://dx.doi.org/10.1016/j.matpr.2021.03.609.

[4] Manu T, Nazmi Ali Reza, Shahri Bahareh, Emerson Nick, Huber Tim. Biocomposites: A review of materials and perception. Mater Today Commun 2022;31(February):103308. http://dx.doi.org/10.1016/j.mtcomm.2022.103308.

[5] Residori Sara, Dul Sithiprumnea, Pegoretti Alessandro, Fambri Luca, Pugno Nicola M. Three dimensional printing of multiscale carbon fiber-reinforced polymer composites containing graphene or carbon nanotubes. Nanomaterials 2022;12(12). http://dx.doi.org/10.3390/nano12122064.

[6] Li Yan, Zhang Han, Crespo Maria, Porwal Harshit, Picot Olivier, Santagiuliana Giovanni, et al. In situ exfoliation of graphene in epoxy resins: A facile strategy to efficient and large scale graphene nanocomposites. ACS Appl Mater Interf 2016;8(36):24112–22. http://dx.doi.org/10.1021/acsami.6b07492.

[7] Gong Ying, Liu Andong, Yang Guisheng. Polyamide single polymer composites prepared via in situ anionic polymerization of $\epsilon$-caprolactam. Composites A 2010;41(8):1006–11. http://dx.doi.org/10.1016/j.compositesa.2010.04.006.

[8] Gucma Maciej, Bryll Katarzyna, Gawdzinska Katarzyna, Przetakiewicz Wojciech, Piesowicz Elzbieta. Technology of single polymer polyester composites and proposals for their recycling. Sci J Maritime Univ Szczecin-Zeszyty Naukowe Akad Morskiej W Szczecinie 2015;44(116):14–8. http://dx.doi.org/10.17402/050.

[9] Cabrera N, Alcock B, Loos J, Peijs T. Processing of all-polypropylene composites for ultimate recyclability. Proc Inst Mech Eng L 2004;218(2):145–55. http://dx.doi.org/10.1243/146442004323085563.

[10] Yu Long, Dean Katherine, Li Lin. Polymer blends and composites from renewable resources. Progr Polymer Sci (Oxford) 2006;31(6):576–602. http://dx.doi.org/10.1016/j.progpolymsci.2006.03.002.

[11] Shields RJ, Bhattacharyya D, Fakirov S. Fibrillar polymer-polymer composites: Morphology, properties and applications. J Mater Sci 2008;43(20):6758–70. http://dx.doi.org/10.1007/s10853-008-2693-z.

[12] Karger-Kocsis J, Bárány T. Single-polymer composites (SPCs): Status and future trends. Compos Sci Technol 2014;92:77–94. http://dx.doi.org/10.1016/j.compscitech.2013.12.006.

[13] Zhang Liying, Qin Yijing, Zheng Guoqiang, Dai Kun, Liu Chuntai, Yan Xingru, et al. Interfacial crystallization and mechanical property of isotactic polypropylene based single-polymer composites. Polymer 2016;90:18–25. http://dx.doi.org/10.1016/j.polymer.2016.02.052.

[14] Fakirov Stoyko. Nano- and microfibrillar single-polymer composites: A review. Macromol Mater Eng 2013;298(1):9–32. http://dx.doi.org/10.1002/mame.201200226.

[15] Gawdzinska Katarzyna, Nabialek Marcin, Sandu Andrei Victor, Bryll Katarzyna. The choice of recycling methods for single-polymer polyester composites. Mater Plast 2018;55:658–65. http://dx.doi.org/10.37358/mp.18.4.5096.

[16] Dorigato Andrea, Pegoretti Alessandro. Biodegradable single-polymer composites from polyvinyl alcohol. Colloid Polymer Sci 2012;290(4):359–70. http://dx.doi.org/10.1007/s00396-011-2556-z.

[17] Alcock B, Cabrera NO, Barkoula NM, Loos J, Peijs T. The mechanical properties of unidirectional all-polypropylene composites. Composites A 2006;37(5):716–26. http://dx.doi.org/10.1016/j.compositesa.2005.07.002.

[18] Matabola KP, De Vries AR, Moolman FS, Luyt AS. Single polymer composites: A review. J Mater Sci 2009;44(23):6213–22. http://dx.doi.org/10.1007/s10853-009-3792-1.

[19] Liu Qingsheng, Zhao Mingming, Zhou Yuqi, Yang Qibing, Shen Ying, Gong R Hugh, et al. Polylactide single-polymer composites with a wide melt-processing window based on core-sheath PLA fibers. Mater Des 2018;139:36–44. http://dx.doi.org/10.1016/j.matdes.2017.10.066.

[20] Bhattacharyya D, Maitrot P, Fakirov S. Polyamide 6 single polymer composites. Expr Polymer Lett 2009;3(8):525–32. http://dx.doi.org/10.3144/expresspolymlett.2009.65.

[21] Alcock Ben, Peijs Ton. Technology and development of self-reinforced polymer composites. Adv Polymer Sci 2013;251(April 2019):1–76. http://dx.doi.org/10.1007/12_2011_159.

[22] Bárány Tamás, Izer András, Czigány Tibor. High performance self-reinforced polypropylene composites. Mater Science Forum 2007;537–538:121–8. http://dx.doi.org/10.4028/www.scientific.net/msf.537-538.121.

[23] Wright-Charlesworth Debra D, Peers William J, Miskioglu Ibrahim, Loo Laura L. Nanomechanical properties of self-reinforced composite poly(methyl methacrylate) as a function of processing temperature. J Biomed Mater Res A 2005;74(3):306–14. http://dx.doi.org/10.1002/jbm.a.30226.

[24] Andrzejewski Jacek, Barczewski Mateusz. Single polymer composites as replacement for glass fiber (April). 2013, p. 1–4.

[25] Raju Benjamin, Hiremath SR, Roy Mahapatra D. A review of micromechanics based models for effective elastic properties of reinforced polymer matrix composites. Compos Struct 2018;204(July):607–19. http://dx.doi.org/10.1016/j.compstruct.2018.07.125.

[26] Wu Y, Ju JW. Elastoplastic damage micromechanics for continuous fiber-reinforced ductile matrix composites with progressive fiber breakage. Int J Damage Mech 2017;26(1):3–27. http://dx.doi.org/10.1177/1056789516655671.

[27] Massarwa Eyass, Aboudi Jacob, Haj-Ali Rami. A multiscale progressive damage analysis for laminated composite structures using the parametric HFGMC micromechanics. Compos Struct 2018;188(January):159–72. http://dx.doi.org/10.1016/j.compstruct.2017.11.089.

[28] Haj-Ali Rami. Cohesive micromechanics: A new approach for progressive damage modeling in laminated composites. Int J Damage Mech 2009;18(8):691–719. http://dx.doi.org/10.1177/1056789508096560.

[29] Dutta Sudakshina, Chandra Kishen JM. Progressive damage through interface microcracking in cementitious composites: A micromechanics based approach. Int J Solids Struct 2018;150:230–40. http://dx.doi.org/10.1016/j.ijsolstr.2018.06.017.

[30] Moncada Albert M, Chattopadhyay Aditi, Bednarcyk Brett A, Arnold Steven M. Micromechanics-based progressive failure analysis of composite laminates using different constituent failure theories. J Reinf Plast Compos 2012;31(21):1467–87. http://dx.doi.org/10.1177/0731684412456330.

[31] Wan Lei, Ismail Yaser, Sheng Yong, Ye Jianqiao, Yang Dongmin. A review on micromechanical modelling of progressive failure in unidirectional fibre-reinforced composites. Composit C: Open Access 2023;10(October 2022):100348. http://dx.doi.org/10.1016/j.jcomc.2023.100348.

[32] Curtin William A. Theory of mechanical properties of ceramic-matrix composites. J Am Ceram Soc 1991;74(11):2837–45. http://dx.doi.org/10.1111/j.1151-2916.1991.tb06852.x.

[33] Curtin WA. Ultimate strengths of fibre-reinforced ceramics and metals. Composites 1993;24(2):98–102. http://dx.doi.org/10.1016/0010-4361(93)90005-S.

[34] Curtin WA, Zhou SJ. Influence of processing damage on performance of fiber-reinforced composites. J Mech Phys Solids 1995;43(3):343–63. http://dx.doi.org/10.1016/0022-5096(94)00077-I.

[35] Curtin WA. Stochastic damage evolution and failure in fiber-reinforced composites. Adv Appl Mech 1998;36(C):163–253. http://dx.doi.org/10.1016/S0065-2156(08)70186-8.

[36] Foster GC, Ibnabdeljalil M, Curtin WA. Tensile strength of titanium matrix composites: direct numerical simulations and analytic models. Int J Solids Struct 1998;35(19):2523–36. http://dx.doi.org/10.1016/S0020-7683(97)00148-0, URL http://dx.doi.org/10.1016/S0020-7683(97)00148-0.

[37] Kelly A, Davies GJ. The principles of the fibre reinforcement of metals. Metall Rev 1965;10(1):1–77. http://dx.doi.org/10.1179/mtlr.1965.10.1.1.